Petroleum Science 23 (2026) 5292–5318

Contents lists available at ScienceDirect

Petroleum Science

journal homepage: www.keaipublishing.com/en/journals/petroleum-science

Original Paper

Micron- to meter-scale shale oil migration differentiation and mobility effects: New insights into high-mobility migration sweet spot and sustainable shale oil recovery

Fu-Wei Wang [a,b,c,*], Ru-Kai Zhu [d,e], Dong-Xia Chen [f,g,**], Bin Bai [d,e], Chang Liu [d,e], Meng-Ya Jiang [h,i], Ren-Zeng Wanma [j], Qiao-Chu Wang [f,g], Yu-Chao Wang [f,g], Lan-Xi Rong [f,g], Yu-Qi Wang [f,g], Chen Liu [f,g], Khawaja-Hasnain Iltaf [k], Zhang-Xin Chen [l,m]

[a] College of Geophysics, Chengdu University of Technology, Chengdu, 610059, Sichuan, China
[b] Key Lab of Earth Exploration & Information Techniques of Ministry of Education, Geophysical Institute, Chengdu University of Technology, Chengdu, 610059, Sichuan, China
[c] State Key Laboratory of Oil and Gas Reservoir Geology and Exploitation, Chengdu University of Technology, Chengdu, 610059, Sichuan, China
[d] PetroChina Research Institute of Petroleum Exploration and Development, Beijing, 100083, China
[e] State Key Laboratory of Continental Shale Oil, Daqing, 163712, Heilongjiang, China
[f] State Key Laboratory of Petroleum Resources and Engineering, China University of Petroleum (Beijing), Beijing, 102249, China
[g] College of Geosciences, China University of Petroleum (Beijing), Beijing, 102249, China
[h] Research Institute of Exploration and Development, PetroChina Changqing Oilfield Company, Xi'an, 710018, Shaanxi, China
[i] National Engineering Laboratory for Exploration and Development of Low-Permeability Oil & Gas Fields, Xi'an, 710018, Shaanxi, China
[j] Taibailiang Operation Area, No. 11 Oil Production Plant, Changqing Oilfield Branch, Qingyang, 745108, Gansu, China
[k] Department of Earth and Environmental Sciences, The University of Texas at Arlington, TX, 76019, USA
[l] Chemical and Petroleum Engineering, Schulich School of Engineering, University of Calgary, Calgary, T2N 1N4, Canada
[m] Ningbo Institute of Digital Twin, Eastern Institute of Technology, Ningbo, 315200, Zhejiang, China

ARTICLE INFO

Article history:
Received 4 August 2025
Received in revised form
4 January 2026
Accepted 10 July 2026
Available online 15 July 2026

Edited by Xiu-Fang Hu

Keywords:
Shale oil systems
Migration differentiation
Mobility effects
Micron-to-meter scale
Multimethod combination
Triassic Chang 7 Member shale

ABSTRACT

Understanding multiscale migration differentiation within shale oil systems is critical for identifying high-mobility migration sweet spots that facilitate the sustainable shale oil recovery. However, owing to geological complexity and technical uncertainty, the chemical differentiation and mobility effects of shale oil migration have not been clarified. This study is focused on elucidating the μm–m-scale migration differentiation and mobility effects in shale oil systems by combining multiple methods, including laser scanning confocal microscopy (LSCM), nuclear magnetic resonance (NMR), multi-temperature pyrolysis, and extract geochemical analysis. Core samples collected nearly equidistantly from the Triassic Chang 7 Member shale system in the Ordos Basin are employed for investigation. The LSCM results reveal that interlaminar shale oil migration on the μm–mm scale manifests in the form of light/heavy component differentiation. However, cm–m-scale migration across laminae assemblages (or lithofacies) corresponds to pyrolysis parameter anomalies, original–true hydrocarbon generation potential differences, chemical compositions and n-alkane differentiation. The migration hydrocarbon inputs can improve the *in situ* oil composition and movable oil content, thus affecting shale oil mobility. The mobility disparities between source–reservoir units in a shale oil system are primarily controlled by the degree of migration differentiation. Notably, the good source–good reservoir laminated units at the μm–mm scale and the thick source–thick reservoir configurations at the cm–m scale exhibit relatively strong migration differentiation and favorable mobility improvement. These mobility patterns associated with μm–m migration differentiation are critical for evaluating high-mobility sweet spots and developing cost-effective and sustainable shale oil systems.

* Corresponding author.
** Corresponding author.
E-mail addresses: wangfw@cdut.edu.cn (F.-W. Wang), lindachen@cup.edu.cn (D.-X. Chen).
Peer review under the responsibility of China University of Petroleum (Beijing).

https://doi.org/10.1016/j.petsci.2026.07.021

1. Introduction

In petroliferous basins worldwide, hydrocarbon migration differentiation is inevitable in the formation of giant oil–gas pools, which is manifested primarily by variations in the physical and chemical properties of hydrocarbons migrating along rock pores (McAuliffe, 1979; Schowalter, 1979; Krooss et al., 1991; Larter et al., 1996; Sivan et al., 2008; Zhang et al., 2013). In recent decades, in the oil–gas industry, the migration of hydrocarbons expelled from the source rock to the adjacent permeable carrier bed (i.e., primary migration) (Bray and Foster, 1980; Leythaeuser et al., 1982; Stainforth and Reinders, 1990; Lafargue et al., 1994) and the migration of hydrocarbons along the carrier bed from the source area to the trap (i.e., secondary migration) (McAuliffe, 1979; Schowalter, 1979; Dembicki and Anderson, 1989; Krooss et al., 1991; George et al., 2004) have been thoroughly studied. Accordingly, these findings have helped elucidate the hydrocarbon accumulation mechanisms in conventional and tight oil–gas systems, significantly advancing the discovery of giant oil–gas fields worldwide (Hao et al., 2007, 2010; Zhu et al., 2020). However, because a shale oil system has long been regarded as self-generating and self-storing, migration differentiation has not received sufficient attention. Recently, exploration practices have confirmed the objective existence of multiscale migration in shale oil systems, revealing that organic-lean shale formations are more enriched in movable oil than organic-rich shale formations are (Hwang et al., 2002; Han et al., 2015; Gao et al., 2024; Hu et al., 2024a, 2024b, 2025). Identifying the high-mobility interval within shale systems has always been a key challenge in evaluating shale sweet spots and improving the economic recovery of shale oil resources. Thus, shale oil migration differentiation and the corresponding mobility effects urgently need to be investigated, which is crucial for revealing novel high-mobility migration sweet spots in shale oil systems that are completely different from traditional in situ sweet spots.

Unlike the hundred-meter- to kilometer-scale migration in conventional and tight oil–gas systems, detectable migration distances in shale oil systems are much shorter and primarily range from the μm scale to the m scale (Han et al., 2015; Gao et al., 2024). Shale oil migration essentially results from hydrocarbon flow under different source–reservoir configurations in a shale system, which manifests as oil migration between laminates, interbeds or lithofacies with different hydrocarbon generation/storage capabilities (Gao et al., 2024; Hu et al., 2024a, 2024b). Correspondingly, the migration distance of a shale formation varies for specimens with different source–reservoir configurations. Specifically, pure shale and laminated-type shale formations characterized by source–reservoir coexistence, such as the Eagle Ford Formation in the Gulf of Mexico Basin (Edman and Pitman, 2010; Ko et al., 2017; González-Betancourt et al., 2022), the Qingshankou Formation in the Songliao Basin (Liu et al., 2019; He et al., 2022; Zhang et al., 2023), and the Shahejie Formation in the Bohai Bay Basin (Li et al., 2016; Wang et al., 2019; Li, 2020; Liang et al., 2022), usually undergo oil migration at the μm–mm scale. In terms of the sandwich-type shale formations characterized by source–reservoir interbedding or separation, such as the Bakken shale in the Williston Basin (Jarvie et al., 2011; Al Duhailan and Sonnenberg, 2014; Hawthorne et al., 2021) and the Triassic Chang 7 Member of the Ordos Basin (Zou et al., 2019; Guo et al., 2022; Yuan et al., 2023), the detectable oil migration distance is greater and predominantly at the cm–m scale. These shale oil migration phenomena across the μm–m scale tend to affect oil mobility because of the chemical composition changes caused by migration differentiation. Theoretically, polar components with poor transport capacity (e.g., nonhydrocarbons and asphaltenes) usually remain in the organic-rich layer in an adsorbed state, whereas nonpolar hydrocarbon components (e.g., saturate and aromatic hydrocarbons) that exhibit better mobility preferentially flow into the organic-lean layer in a free state (Charlesworth, 1986; Brother et al., 1991; Bennett et al., 2002; Ataman et al., 2016). However, in practice, accurately characterizing these μm–m-scale migration differentiations and mobility effects in shale oil systems is challenging because of their geological complexity and technical uncertainty.

Methods for characterizing conventional hydrocarbon migration differentiation face challenges in their applicability to understanding shale oil migration over short distances (Gao et al., 2024; Hu et al., 2025). To this end, scholars have implemented microscopic observations, experimental analyses, and physical and numerical simulations to investigate the migration differentiation associated with shale oil. Specifically, microscopic observation methods primarily employ fluorescent thin sections and laser scanning confocal microscopy (LSCM) to characterize the morphological characteristics of the oil present in shale pores directly (Gao et al., 2023), which enables a qualitative understanding of μm–mm-scale oil migration with high resolution. However, the shortcoming of microscopic observations is their inability to provide quantitative information on oil geochemistry and their inability to implement dynamic process monitoring. In contrast, experimental analysis methods mainly include solvent extraction, gas chromatography–mass spectrometry (GC–MS) (Poetz et al., 2020; Vanini et al., 2020; Yuan et al., 2023), carbon isotope analysis (Simonet et al., 1981; Clayton and Bostick, 1986; Hu et al., 2018; Wang et al., 2020), and Rock–Eval pyrolysis experiments (Zou et al., 2019; Hu et al., 2024a, 2024b) to quantitatively describe the geochemical differentiation events that are related to shale oil migration. These methods can be used to effectively reveal the variations in oil components, biomarkers, isotopes, free oil contents, and hydrocarbon expulsion efficiencies at the cm–m scale (Zhang et al., 2017; Zou et al., 2019; Hu et al., 2020). However, such methods tend to damage the initial structure of shale during sample preparation and experiments, resulting in the loss of spatial resolution and the inability to provide microscale information. In addition, physical simulations combined with online NMR imaging and online CT techniques have been employed to investigate hydrocarbon migration pathways in tight sandstone reservoirs (Zheng et al., 2016; Arshadi et al., 2018; Zhao et al., 2020a, 2020b; Cui et al., 2022; Zhang et al., 2024); however, physical simulations of ultralow-permeability shale are relatively rare because of the high cost. Owing to the advantages of being more cost-effective and less time-consuming, numerical methods, such as pore networks (Xiong et al., 2016; Zhao et al., 2020a), lattice Boltzmann (Guo and Shu, 2013; Zhao et al., 2020a), and molecular dynamics (Zhang et al., 2020), have been adopted to reveal dynamic fluid flow behaviors in porous media. However, current numerical simulations typically simulate fluid flow within a single type of pore or within a simple pore network, but they face challenges in simulating hydrocarbon migration in highly heterogeneous pore networks of shale, especially in terms of accurately reflecting the oil composition or geochemical differentiation characteristics.

Furthermore, precise characterization of shale pore-fracture systems and fluid mobility is essential for an in-depth understanding of the shale oil migration mechanism (Guo et al., 2024; Sun et al., 2024). The pore structure of shale reservoirs can be quantitatively evaluated through fluid intrusion methods, which generally include helium pycnometry, fluid saturation, mercury intrusion, and gas physisorption (Anovitz and Cole, 2015; Sun

et al., 2020). These methods are utilized to probe pore structure in shale reservoirs by injecting small molecular fluids such as helium, water, mercury, nitrogen, carbon dioxide, argon, etc. (Thommes et al., 2015; Mastalerz et al., 2021; Wang and Cheng, 2023; Zhao et al., 2023). On the other hand, the pore structure can also be observed by radiation methods, which are utilized for imaging observations through the interaction of light, electrons, ions, and X-ray with the surface or the whole of the shale (Curtis et al., 2012; Milliken et al., 2013; Sun et al., 2024). Due to the different observation principles, the characterization scales and sample fields of view corresponding to different methods also vary. Meanwhile, the pore network structure of shale can also be characterized by neutron and X-ray scattering as well as nuclear magnetic resonance of hydrogen atoms (Hosseini et al., 2021; Elsayed et al., 2022). Regarding the evaluation of shale oil mobility, NMR technology is widely utilized to distinguish the occurrence states of different fluids within shale, including free fluids (e.g., movable oil) and bound fluids (e.g., adsorbed oil) (Li et al., 2020; Liu et al., 2020). However, NMR cannot distinguish the chemical compositions of hydrocarbons or quantitatively describe the mobile oil content. In comparison, multi-temperature pyrolysis, which has the advantages of low cost and is suitable for batch sample analysis, is usually employed to quantify the movable oil content or percentage in shale (Jiang et al., 2016). Nevertheless, the complexity of multiscale migration and mobility makes it challenging to thoroughly evaluate shale oil migration and mobility characteristics by using a single method (or tool), resulting in an insufficient understanding of the mobility effects caused by migration differentiation. Thus, combining multiple methods to compensate for their respective shortcomings is essential for fully revealing multiscale shale oil migration differentiation and mobility variations, thereby providing a scientific basis for migration sweet spot evaluation and drilling decision-making in shale oil systems.

The objective of this investigation is to systematically elucidate μm–m-scale migration differentiation and its corresponding mobility effects in shale oil systems by combining multiple methods and tools. In this study, the basic geological, geochemical and oil-containing characteristics of shale were first characterized by thin-section, scanning electron microscopy (SEM), QEMSCAN, X-ray diffraction (XRD), total organic carbon (TOC), Rock–Eval pyrolysis, and N_2 adsorption. Subsequently, shale oil migration events, differentiation characteristics and mobility effects were investigated primarily by combining laser scanning confocal microscopy (LSCM), nuclear magnetic resonance (NMR), multi-temperature pyrolysis, and extract geochemical analysis. This study relied on core samples of the Triassic Chang 7 Member lacustrine shale system in the Ordos Basin, China, especially the Chang 7_3 submember shale, to characterize the shale oil migration differentiation and mobility effects in detail. This study can improve the understanding of oil migration behavior, chemical differentiation, and associated mobility variations in shale systems, which is critical for assessing future high-mobility migration sweet spots and enabling cost-effective and sustainable shale oil development.

2. Materials and methods

2.1. Sample collection

The Triassic Chang 7 lacustrine shale in the Ordos Basin, the largest shale oil production base in China, was selected as the target shale interval in this study (Fig. 1) (Tao et al., 2023). Well H-261, a vertical exploration well located in the northern part of the Chang 7 shale sedimentary area, was used as a sampling well (Fig. 1(c)). The shale formations in this well were composed of the lower Chang 7_3 submembers, the Chang 7_2 submembers and the upper Chang 7_1 submembers (Fig. 1(d)) (Wang et al., 2022a, 2022b, 2025). Among these samples, the thick black shale in the Chang 7_3 submember was designed to be the focus of the shale oil experiment. In this investigation, a total of 56 core samples were collected nearly equidistantly from this well at a rate of three samples per meter. Specifically, bulk/columnar core samples were systematically prepared for thin-section, SEM, QEMSCAN, LSCM and two-dimensional T_1–T_2 NMR analyses. Sample powders were subjected to TOC, XRD, N_2 adsorption, Rock–Eval pyrolysis and multi-temperature pyrolysis measurements. Additionally, extracts from rock samples were subjected to component fractionation and gas chromatography–mass spectrometry (GC–MS) experiments. The sample preparation process and the entire workflow used in this study are described in Fig. 2.

2.2. Methods

2.2.1. Thin-section, SEM, QEMSCAN, and XRD analyses

To characterize the shale petrological and lamination characteristics effectively, core samples were polished or ground to obtain a flat and smooth surface for thin-section, SEM and QEMSCAN observations. Thin-section analysis was performed under both single-polarized and ortho-polarized light at magnifications ranging from 20 to 600 times. SEM analysis was conducted at the China University of Petroleum (Beijing) using a ZEISS Crossbeam 540 SEM, which had an electron beam resolution of 0.9 nm at 15 kV and 1.8 nm at 1 kV. These SEM images were used to reveal the two-dimensional mineral morphological and pore structure characteristics of the shale. Moreover, QEMSCAN was applied to scan the preset surface area with a high-energy electron beam and subsequently obtain a color map of the mineral assemblage. This instrument detected the contents of elements and minerals by combining the grayscale of the backscattered electron (BSE) image with the intensity of X-rays. For the XRD experiments, the collected samples were ground into powder with an agate mortar and sieved through 75-μm filters to facilitate mineralogy testing. After the powder was fed into the instrument, the output diffractograms were analyzed by a computer to identify minerals and consequently calculate the weight percentage of each mineral.

2.2.2. TOC measurement and Rock–Eval pyrolysis

For the purpose of organic feature evaluation, TOC analysis of 56 samples was performed at the State Key Laboratory of Petroleum Resources and Engineering of the China University of Petroleum (Beijing) using a LECO CS230HC carbon-sulfur analyzer. Prior to the experiment, the samples being evaluated were pulverized into 100–200-mesh powder. To remove carbonate minerals and moisture, the sample powder was treated with a 12.5% hydrochloric acid solution for 24 h to remove inorganic carbon and subsequently burned with a high-temperature oxygen stream to measure the TOC content.

These samples were analyzed using a Rock–Eval pyrolyzer (Rock–Eval 6) according to the GB/T18602-2012 standard technique (National Standards Complication Group of People's Republic of China, 2012). For powder samples that were pulverized into sizes of 100 mesh, approximately 100 mg of each sample was heated to 650 °C in a nitrogen atmosphere at a heating rate of 25 °C/min. During the heating process, the quantity of free hydrocarbons (S_1) was obtained by heating the powder at 300 °C for 3 min, and the residual hydrocarbon generation potential (S_2) was detected at pyrolysis temperatures ranging from 300 °C to 600 °C at a heating rate of 25 °C/min. The temperature of maximum

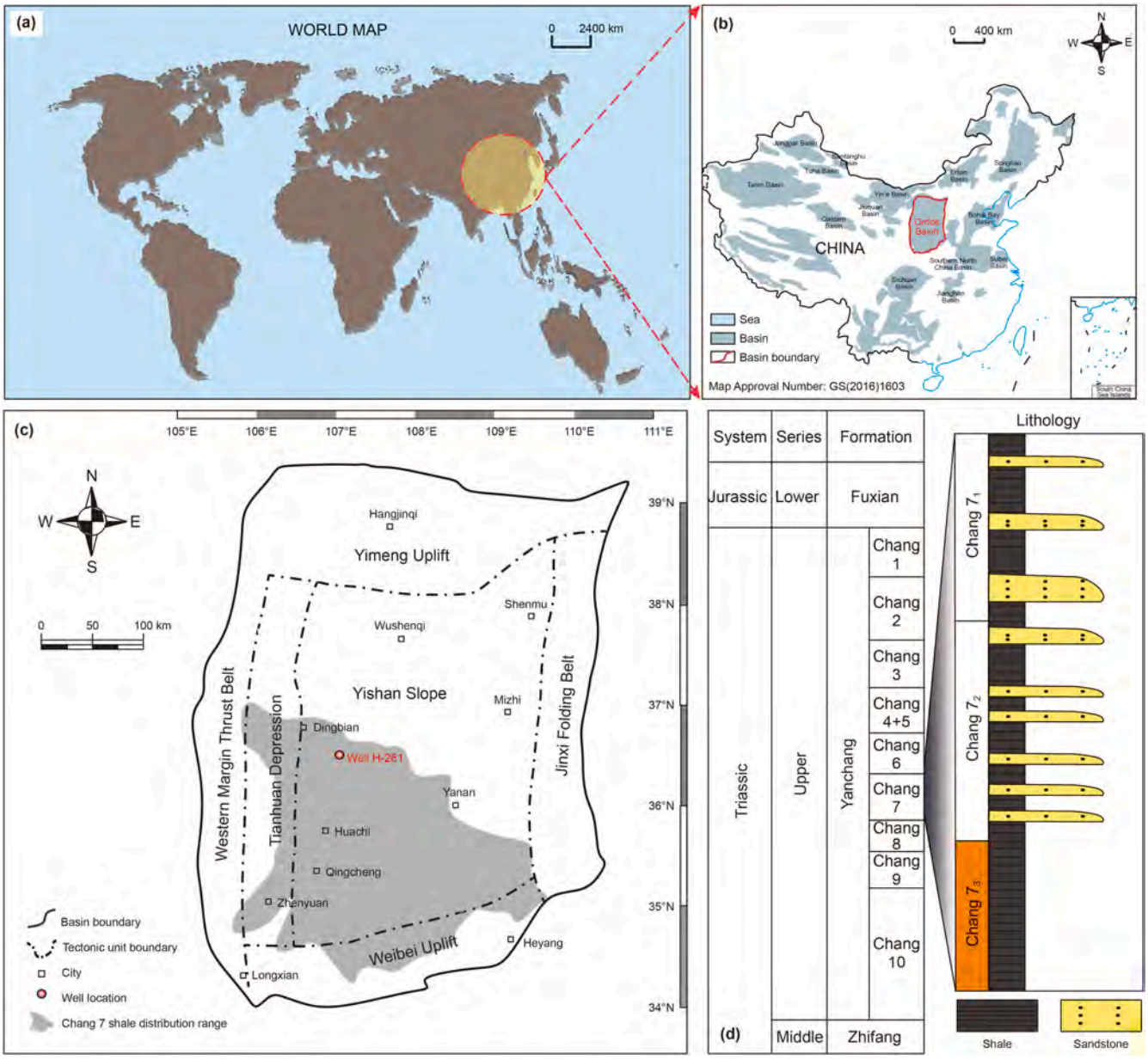

Fig. 1. Maps showing **(a)** the location of China, **(b)** the sedimentary basins in China and the location of the Ordos Basin (Tao et al., 2023), **(c)** the tectonic units of the Ordos Basin and the location of Well H-261 for core samples, and **(d)** the generalized Triassic Yanchang Formation stratigraphy and Chang 7 lacustrine shale system (Wang et al., 2022a, 2022b).

hydrocarbon generation corresponding to the S_2 peak (i.e., T_{max}) could be obtained through this experiment. The hydrogen index (HI = S_2 × 100/TOC) of each shale sample was consequently quantified.

2.2.3. N_2 adsorption, solvent extraction, fractionation, and gas chromatography–mass spectrometry (GC–MS)

To quantitatively assess the pore structure of the shale, N_2 adsorption experiments were conducted at the China University of Petroleum (Beijing) using an ASAP2020KM+C (Micromeritics, USA) automatic specific surface area analyzer and porosity analyzer. This instrument could measure apertures ranging from 0.35 nm to 500 nm, with a minimum detection surface area of 0.0001 m^2/g and a minimum detection pore volume of 0.0001 cm^3/g. The samples crushed to approximately 0.2 mm were vacuum-dried at 80 °C for 12 h and subsequently tested with 99.99% pure nitrogen at 77 K (−196.15 °C). In accordance with the adsorbed nitrogen quantity, the surface area was calculated by the Brunauer–Emmett–Teller (BET) method (Brunauer et al., 1938), and the pore volume and pore size parameters were determined by the Barrett–Joyner–Halenda (BJH) method (Barrett et al., 1951).

For geochemical analysis, the shale samples were crushed to sizes of less than 100 mesh and extracted with chloroform in a Soxhlet extractor for 72 h according to the SY/T5119-2016 (National Energy Administration, 2016) standard technique. After the asphaltene was precipitated by n-hexane, the soluble components in the extract were subsequently separated through a silica–alumina chromatographic column (silica:alumina = 3:1), where the saturate hydrocarbons and aromatics were washed out by using n-hexane and dichloromethane, respectively. Accordingly, the relative contents of saturate hydrocarbon, aromatic hydrocarbon, nonhydrocarbon and asphaltene components in the

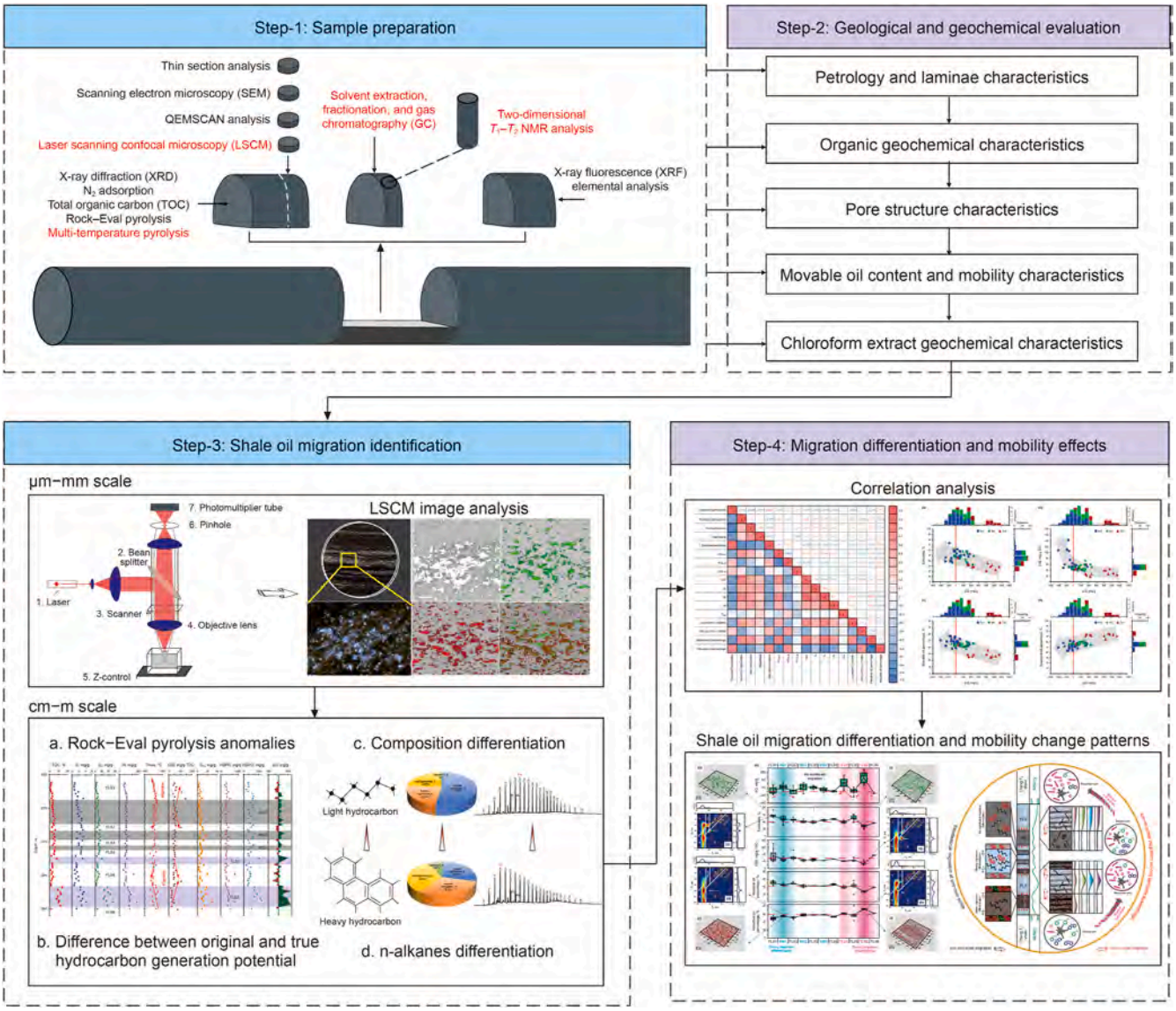

Fig. 2. Schematic diagram showing the entire workflow in this study.

chloroform extract were obtained. Moreover, the saturate hydrocarbon components were put into a gas chromatography–mass spectrometry (GC–MS)-coupled instrument (Agilent-7890B-5977A) for gas chromatography–mass spectrometry analysis, which consequently detected n-alkane biomarkers.

2.2.4. T_1–T_2 NMR, LSCM, and multi-temperature pyrolysis

To facilitate NMR testing, standard plunger samples with diameters of approximately 25 mm were drilled using wire cutting from the analyzed shale cores. T_1–T_2 NMR experiments were conducted at the State Key Laboratory of Petroleum Resources and Engineering of China University of Petroleum (Beijing) using a high-temperature and high-pressure displacement NMR analysis and imaging system (SPEC-RC035). Specifically, the SR–CPMG sequence was adopted for the T_1–T_2 spectrum test with the following test parameters: wait time (TW) of 10 ms, overlay time (NS) of 32, number of echoes (NECH) of 4096, number of reversals (NTI) of 31, and echo interval of 0.07 ms. This echo interval enabled the T_1–T_2 spectra to effectively reflect the NMR response characteristics of pore fluids and solid hydrogen nuclei, including kerogen/solid bitumen, adsorbed oil, movable oil, free water, and structural water.

To characterize the occurrence of light/heavy components of shale oil at the micron scale, laser scanning confocal microscopy was performed on 0.04–0.05-mm shale slices at a temperature of 25 °C and relative humidity of 30%–46% with a maximum imaging resolution of approximately 200 nm using the SP8 model. The LSCM uses a laser with a fixed wavelength of 488 nm to excite the sample, where the light hydrocarbon components (saturate hydrocarbons and some aromatics) produce fluorescence signals in the wavelength range of 490–600 nm, whereas the heavy hydrocarbon components (some aromatics, nonhydrocarbons and asphaltenes) produce fluorescence signals in the wavelength range of 600–800 nm. For the samples in the LSCM system, the incident light spot was set on the focal plane (XY-axis) perpendicular to the microscope optical axis. Firstly, the information obtained by scanning the sample point by point or line by line was analyzed and processed by the computer into a two-dimensional image, which represents the "slice" image of the plane within the focusing thickness range. Subsequently, by using the volume rendering

processing technology of the computer, these multiple XY-plane images captured at different Z-axis positions (along the microscope optical axis) at certain intervals were "stacked" to reconstruct a three-dimensional stereoscopic image of reservoir pores and oil distribution within the scanning area. Finally, the LSCM technology was employed to quantitatively analyze and calculate the obtained three-dimensional rock pores and microscopic oil images, thereby obtaining the three-dimensional quantitative indicators of the oil components in the rock pores, namely the light/heavy component volume percentage.

For the multi-temperature pyrolysis experiments, the powder shale samples were heated with a Rock–Eval 6 pyrolyzer at a heating rate of 25 °C/min. The detectable $S'_{1\text{-}1}$ was measured when the temperature was increased to 200 °C and maintained for 1 min. Then, the temperature was increased to 350 °C and held for 1 min to identify the produced $S'_{1\text{-}2}$. To detect the produced $S'_{2\text{-}1}$, the temperature was increased to 450 °C at a heating rate of 25 °C/min and maintained for 1 min. Finally, the temperature was raised to 600 °C and again maintained for 1 min to determine the produced $S'_{2\text{-}2}$. $S'_{1\text{-}1}$ predominantly represents the light oil components that exist in the free state, and $S'_{1\text{-}2}$ is mainly composed of light–medium oil components in the free state. $S'_{2\text{-}1}$ suggests that heavy hydrocarbons and colloidal asphaltenes exist in an adsorbed state. $S'_{2\text{-}2}$ corresponds primarily to the hydrocarbons regenerated by kerogen pyrolysis in the shale samples.

3. Results

3.1. Inorganic composition and lamination characteristics of shale

The mineralogical analysis results for the Chang 7_3 shale sample are shown in Fig. 3(a). The results show that the Chang 7_3 shale is primarily composed of quartz (avg. 36.08%), feldspar (avg. 21.06%), and clay minerals (avg. 35.74%), which are accompanied by small amounts of calcite, dolomite and pyrite. In addition, significant vertical heterogeneity in the mineral composition is observed at sampling depths ranging from 2226.2 m to 2245.0 m.

Core, thin-section, SEM and QEMSCAN analyses reveal detectable laminae types and combinations in the Chang 7_3 shale samples (Fig. 3(b)–(m)). Specifically, three types of μm–mm-scale laminae structures can be identified: organic laminae (OL), felsic laminae (FL) and tuffaceous laminae (TL). OL with a flat and wavy morphology appears dark black in core samples (Fig. 3(c) and (d)) and dark brown under thin-section analysis with single-polarized light (Fig. 3(e)). The mineral composition is characterized by high contents of clay minerals and strawberry-shaped pyrite and a low content of clastic particles (Fig. 3(f) and (g)). Conversely, FL with good continuity appears gray (or grayish white) in the core samples and overlaps with organic laminae to form light–dark bands (Fig. 3(c)). The silt-grade clastic structure with a large particle size can be clearly observed by thin-section and SEM analyses, revealing the mixing of terrigenous clastic quartz, feldspar, clay and carbonate minerals (Fig. 3(h)–(j)). The TL appears as continuous strips of grayish brown and light yellow on the core samples (Fig. 3(d)) and light brown under thin sections with single-polarized light (Fig. 3(k)), indicating an uneven angular pyroclastic distribution visible under SEM (Fig. 3(l)). According to the results of the QEMSCAN analysis, TL has a mineralogical characteristic of relatively high clay mineral content and is accompanied by pyrite (FeS_2), which suggests relatively weak and stable hydrodynamic conditions (Fig. 3(m)).

Furthermore, these laminae are randomly combined in the Chang 7_3 shale to form three categories of laminae assemblage structures: massive structures, OL+FL laminae assemblages and OL+TL laminae assemblages. Specifically, shales with massive structures are defined as massive shales (MSs), which can also be characterized as black shales without continuously overlapping stratified layers; the organic matter mainly consists of scattered and clumped algal debris (Fig. 3(b)). Shales with OL+FL laminae assemblages can be identified as felsic laminated shales (FLSs), exhibiting clear interlaminar boundaries formed by a combination of OL and FL (Fig. 3(c)). The continuous bright FL contains well-sorted quartz particles, and the dark OL is enriched in organic matter. Similarly, shales with OL+TL laminae assemblages have been identified as tuffaceous laminated shales (TLSs), which alternate regularly between black OL and light yellow or grayish brown TL (Fig. 3(d)). Unlike FLS, which has relatively strong terrigenous input and hydrodynamic conditions, the strawberry-shaped pyrite distributed along the OL and TL within the TLS indicates the presence of weak hydrodynamic conditions that are conducive to organic matter enrichment. As shown in Fig. 3(n), there are significant differences in the average contents of different minerals within FLS, MS, and TLS, exhibiting a gradual increase in clay minerals and pyrite, while the contents of quartz and feldspar decrease significantly.

3.2. Organic geochemical characteristics of the shale

The detailed organic geochemical analysis results obtained from the shale samples are shown in Fig. 4. The total organic carbon (TOC) content and potential hydrocarbon generation amount (S_1+S_2) vary widely among the three shale types. MS samples present TOC contents ranging from 0.81% to 10.38% (avg. 4.62%) and S_1+S_2 contents ranging from 3.78 mg/g to 53.33 mg/g (avg. 18.49 mg/g), suggesting that most MS samples have very good hydrocarbon generation potential according to the cross-plot of S_1+S_2–TOC. The HI versus T_{max} plot reveals that MS mainly produces type II_1 and type I kerogen in the mature thermal evolution stage. With respect to the FLS samples, the TOC content ranges from 0.36% to 5.82% (avg. 2.70%), and the S_1+S_2 contents vary from 1.05 mg/g to 26.70 mg/g (avg. 10.40 mg/g), indicating that the FLS samples develop fair, good, and very good source rocks. Moreover, the HI versus T_{max} plot reveals that FLS includes type II_2, type II_1 and type I kerogen in the mature stage. The TLS samples present TOC contents ranging from 1.6% to 14.14% (avg. 9.30%) and S_1+S_2 contents ranging from 4.73 mg/g to 86.47 mg/g (avg. 48.19 mg/g), which can be considered very good source rocks. Additionally, TLSs primarily develop mature type I and type II_1 kerogen according to the HI versus T_{max} plot. In summary, the following organic geochemical features or hydrocarbon generation capacity sequences can be obtained: TLS > MS > FLS.

3.3. Pore structure characteristics of the shale

The detailed pore structure analysis results for the Chang 7_3 shale samples by SEM and N_2 adsorption are shown in Figs. 5 and 6. SEM analysis reveals notable differences in two-dimensional pore features among the MS, TLS and FLS samples. The FLS samples commonly exhibit intragranular dissolution pores and intergranular pores with microfractures that cut through the debris (Fig. 5(a)–(c)). The pores of the TLS samples are primarily composed of pyrite intercrystalline pores and clay mineral intragranular pores with microfractures developed along the laminae (Fig. 5(d)–(f)). The analyzed MS samples exhibit mainly intercrystalline pores and intragranular pores with few organic matter pores. However, the number of microfractures is significantly lower than that in the TLS and FLS samples (Fig. 5(g)–(i)). Additionally, three-dimensional pore features can be detected by N_2 adsorption–desorption curves. According to the classification standard set by IUPAC, the hysteresis loop of the N_2

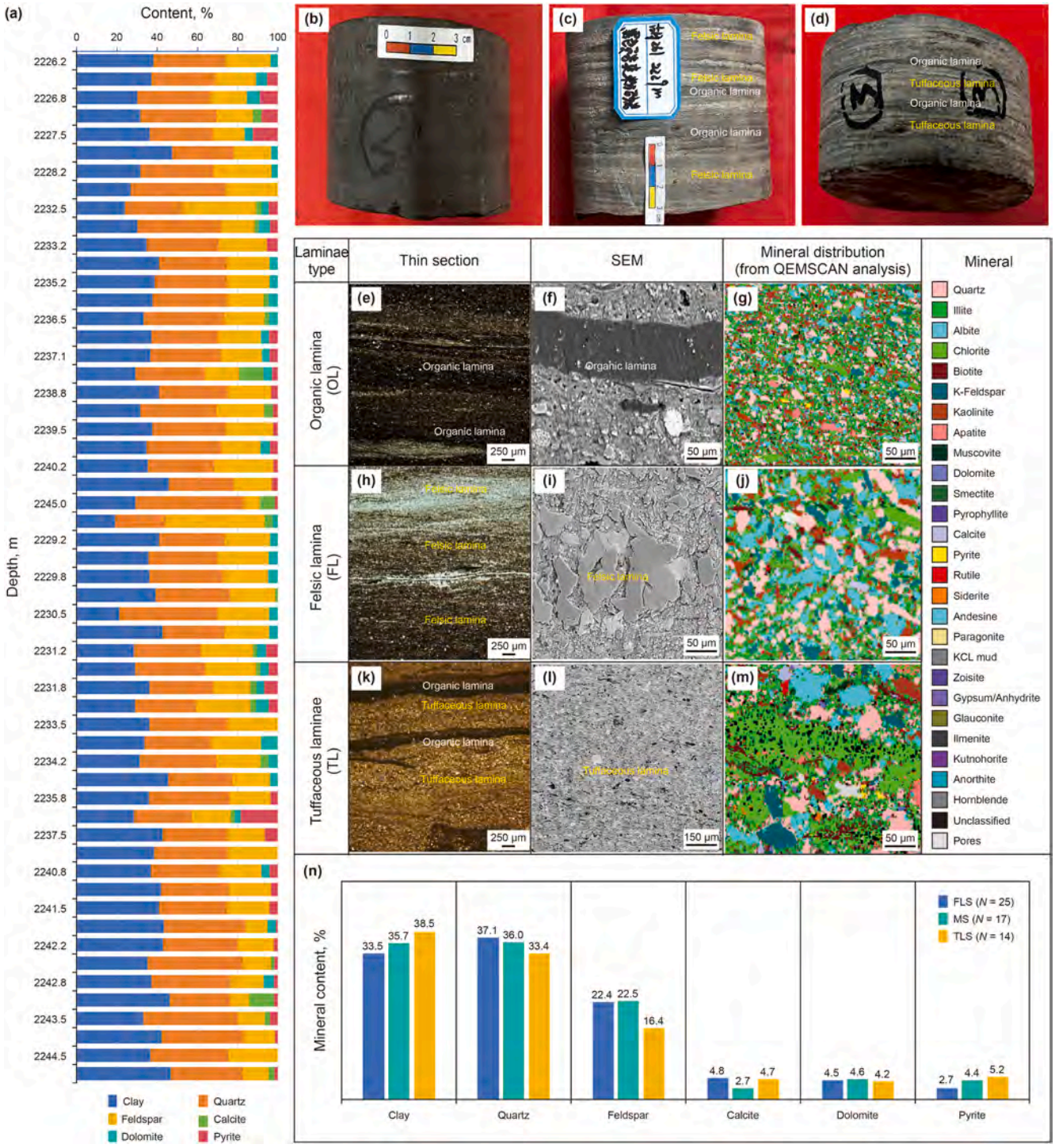

Fig. 3. Mineralogical and laminated structure of the Chang 7_3 shale in the Ordos Basin. **(a)** XRD results showing the mineralogical characteristics of Well H-261 at depths ranging from 2226.2 m to 2245.0 m. **(b)**, **(c)** and **(d)** Typical core photographs showing the massive shale (MS), felsic laminated shale (FLS) and tuffaceous laminated shale (TLS) samples within the Chang 7_3 shale, respectively. **(e)** Organic laminae in plane-polarized light in Well H-261 (2234.5 m). **(f)** SEM image showing the continuous organic laminae and associated strawberry-shaped pyrite in Well H-261 (2243.5 m). **(g)** QEMSCAN image illustrating the mineralogical composition of organic laminae in Well H-261 (2239.2 m). **(h)** Felsic laminae in plane-polarized light in Well H-261 (2234.5 m). **(i)** SEM image showing the continuous felsic laminae dominated by terrigenous clastic particles in Well H-261 (2234.2 m). **(j)** QEMSCAN image showing the mineralogical compositions of the felsic laminae dominated by quartz and feldspar in Well H-261 (2239.2 m). **(k)** Thin sections under plane-polarized light illustrating the alternating distribution of tuffaceous laminae and organic laminae in Well H-261 (2237.1 m). **(l)** SEM image showing the continuous tuffaceous laminae characteristics in Well H-261 (2232.8 m). **(m)** QEMSCAN image showing the mineralogical compositions of tuffaceous laminae dominated by clay minerals in Well H-261 (2232.8 m). **(n)** Comparison of the average contents of different minerals in massive shale (MS), felsic laminated shale (FLS) and tuffaceous laminated shale (TLS).

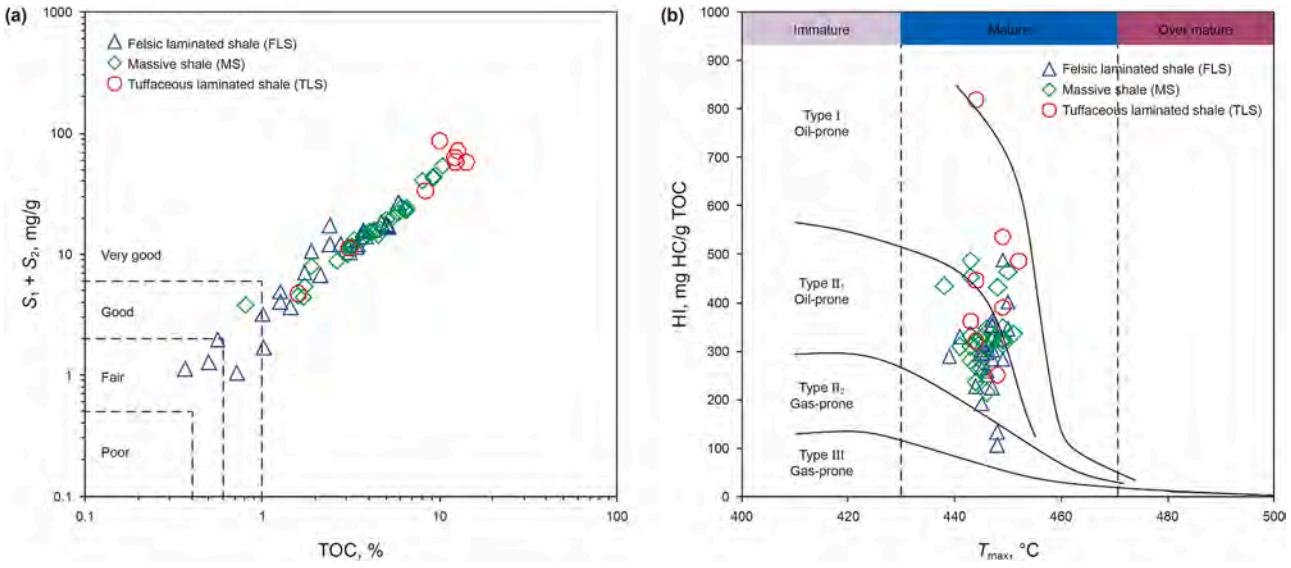

Fig. 4. **(a)** Hydrocarbon generation potential (S_1+S_2) versus TOC plot of the shale samples. **(b)** Cross-plot of the HI–T_{max} values for three lithologies of Chang 7_3 shale in the Ordos Basin. Hydrogen index (HI) = S_2/TOC × 100, mg HC/g TOC.

adsorption–desorption curve can be divided into four types of pore morphology: H1 (cylindrical pores with both open ends), H2 (ink-bottle-shaped pores), H3 (slit-shaped pores) and H4 (narrow-slit-shaped pores) (Broekhoff, 1979; Sing, 1985; Lowell et al., 2004). The N_2 adsorption–desorption curves of the FLS samples are dominated by H2-type with a few H3-type hysteresis loops (Fig. 6(b)), indicating that FLS results in the development of more ink-bottle pores. The N_2 adsorption–desorption curves for the TLS samples exhibit predominantly H3-type hysteresis loops with a few H2-type hysteresis loops (Fig. 6(c)), suggesting that TLS has more parallel slit-shaped pores. In terms of MS, the analyzed samples are primarily characterized by H2 and H3 hysteresis loops (Fig. 6(a)), demonstrating that MS predominantly develops ink-bottle-shaped and slit-shaped pores. Fig. 6(d)–(f) shows the curve of shale pore diameter and cumulative pore volume, which can reflect the contribution of pores of different pore diameters to pore volume. For MS, the cumulative pore volume rises rapidly when the pore diameter is greater than 10 nm, suggesting that pores larger than 10 nm provide the majority of the pore volume. Similarly, the pore volumes of FLS and TLS are mainly provided by pores with diameters of 0–90 nm and >20 nm, respectively. Fig. 6(g)–(i) displays the curve of shale pore size and cumulative specific surface area, which can exhibit the contribution of pores of different pore diameters to specific surface area. Specifically, the specific surface areas of MS, FLS and TLS are primarily provided by pores with diameters of 0–30 nm, 0–20 nm and 0–40 nm, respectively. In this study, the dV/dlg(D)–D differential distribution curve is selected to analyze the pore diameter distribution, where V represents the pore volume, and D represents the pore diameter. The pore diameters of MS are mainly distributed within the range of 2 nm to 150 nm, and the pore volume change rate shows a bimodal and unimodal distribution (Fig. 6(j)). The pore diameter of FLS is primarily distributed from 1.8 nm to 170 nm, and the pore volume change rate shows a bimodal distribution, with the main peak value in the range of 2–5 nm and 20–60 nm (Fig. 6(k)). The pore diameter of TLS is predominantly distributed within the range of 2 nm to 200 nm, and the pore volume change rate exhibits a unimodal distribution, with the main peak value in the range of 20 nm to 90 nm (Fig. 6(l)).

The detailed pore structure quantitative parameters, including the specific surface area, total pore volume and average pore diameter, detected by N_2 adsorption isotherms are listed in Table 1. FLS samples typically feature high specific surface areas, high total pore volumes and low average pore diameters (Fig. 6(e)–(h) and (k)). The quantitative results reveal specific surface area distributions between 0.95 m^2/g and 19.24 m^2/g (avg. 3.64 m^2/g), and the total pore volume ranges from 0.00555 cm^3/g to 0.038 cm^3/g (avg. 0.01088 cm^3/g). The detected average pore diameter for the FLS samples varies between 5.82 nm and 12.46 nm, with an average value of 9.13 nm. Conversely, the pore structures of the TLS samples are characterized by low specific surface area, low total pore volume and high average pore diameter (Fig. 6(f)–(i) and (l)). The measured specific surface areas for the TLS samples vary between 0.35 m^2/g and 9.17 m^2/g (avg. 1.64 m^2/g), and the total pore volumes range from 0.00279 cm^3/g to 0.0181 cm^3/g (avg. 0.00533 cm^3/g). The average pore diameter detected for the TLS samples ranges from 6.65 nm to 14.74 nm, with an average value of 12.07 nm. In terms of the pore structure of MS, the ranges of the specific surface area, total pore volume and average pore diameter are 0.33–9.16 m^2/g (avg. 1.49 m^2/g), 0.00184–0.01812 cm^3/g (avg. 0.00659 cm^3/g), and 6.64–14.45 nm (avg. 10.25 nm), respectively (Fig. 6(d)–(g) and (j)).

The quality of shale oil reservoirs does not solely depend on the excellence of a single pore structure parameter, but rather on whether parameters such as average pore diameter, specific surface area, and total pore volume can effectively coordinate to maximize oil content and fluidity. A favorable shale reservoir must have sufficient storage capacity and superior seepage capacity to ensure that shale oil can be effectively extracted. Specifically, the average pore diameter, specific surface area and total pore volume tend to affect the permeability, adsorption oil storage site, and free oil storage space of shale reservoirs, respectively. Although the average pore size of FLS is slightly lower than that of MS and TLS, its average specific surface area and total pore volume of FLS are more than twice that of MS and TLS (Fig. 7), suggesting that the largest storage space is available for both adsorbed oil and free oil. In the laminated structure, although the nanoscale pores themselves exhibit poor permeability, the densely developed rock

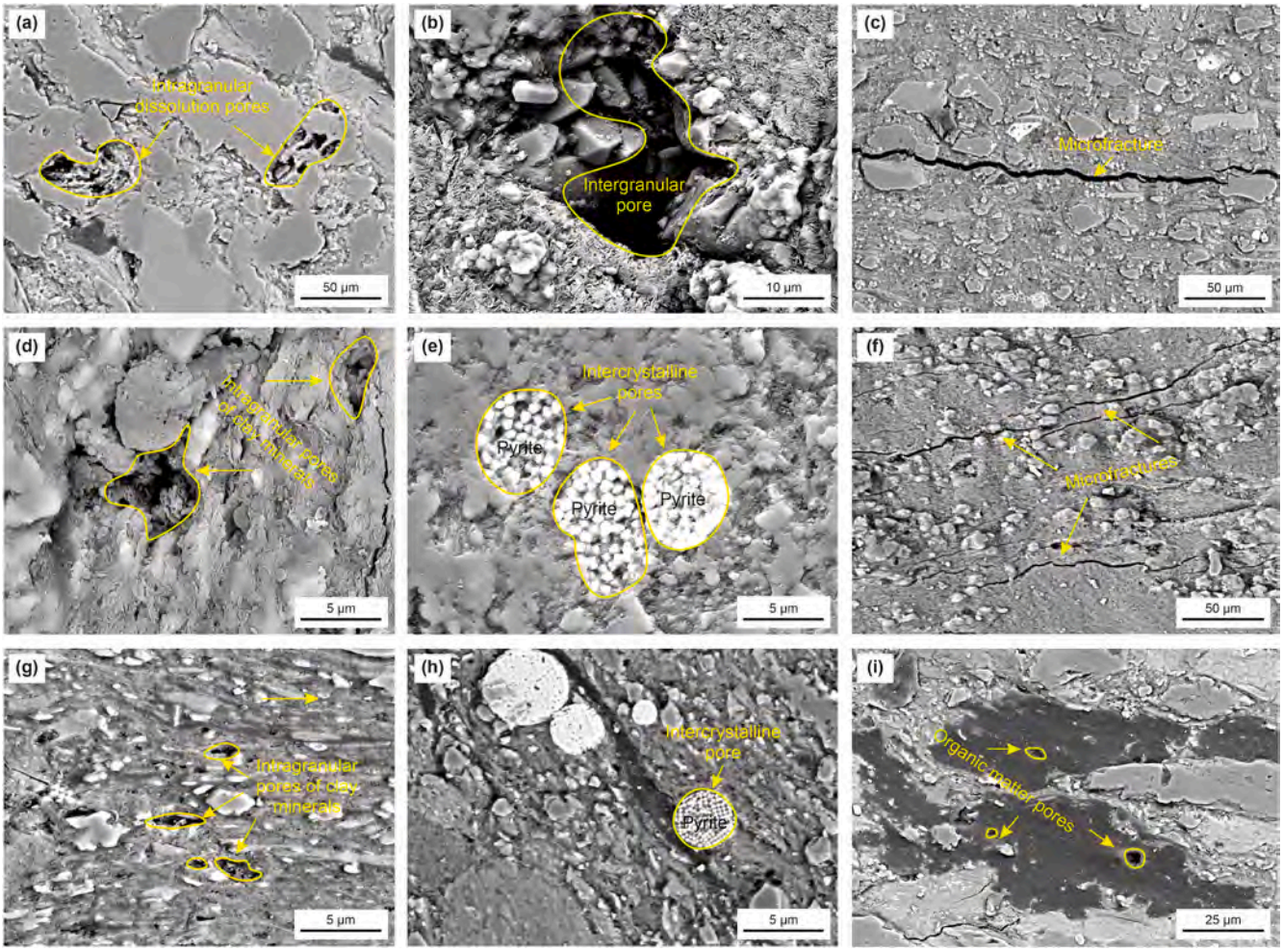

Fig. 5. SEM image showing the pore characteristics of the studied shale samples. **(a)** Intragranular dissolution pores observed in FLS in Well H-261 (2228.5 m). **(b)** SEM image showing an intergranular pore in FLS in Well H-261 (2245 m). **(c)** Microfracture cutting through quartz particles in the felsic laminae of FLS in Well H-261 (2243.5 m). **(d)** Intragranular pores developed in clay minerals in the TLS in Well H-261 (2232.8 m). **(e)** SEM image illustrating the intercrystalline pores in pyrite in the TLS in Well H-261 (2246.5 m). **(f)** Microfractures along the tuffaceous laminae in the TLS in Well H-261 (2246.5 m). **(g)** Intragranular pores of clay minerals in MS in Well H-261 (2243.2 m). **(h)** Intercrystalline pores of pyrite in MS in Well H-261 (2235.5 m). **(i)** Organic matter pores in MS in Well H-261 (2229.5 m). MS = massive shale; FLS = felsic laminated shale; and TLS = tuffaceous laminated shale.

lamellae are natural vulnerable surfaces and percolation dominant channels, especially for FLS with high brittle mineral content, which can appropriately compensate for the seepage disadvantage caused by the relatively small pore diameters. Thus, FLS is a favorable shale reservoir with a relatively balanced storage and seepage. In contrast, TLS, despite exhibiting the largest average pore diameter, has non-negligible shortcomings, that is, the smallest total pore volume and medium-poor specific surface area. This means that the total storage space of TLS is small, and the scale of shale oil that can be stored is very limited. In addition, the high clay mineral content also makes the shale oil within the TLS not easy to flow and exploit. The parameters of MS are balanced and at a medium level, but lack the percolation advantage brought by the laminated structure, therefore the overall quality is at a medium level. In summary, the reservoir quality sequences of different shale types in the study area can be obtained as follows: FLS > MS > TLS.

3.4. Shale movable oil content and mobility characteristics

The movable oil content detected by Rock–Eval pyrolysis and multi-temperature pyrolysis is presented in Fig. 8. The oil saturation index (OSI) is a widely used parameter for evaluating shale oil mobility (Jarvie, 2012) and is defined as the ratio of pyrolysis S_1 (i.e., residual hydrocarbon content in rocks) to total organic carbon content (TOC). According to Rock–Eval pyrolysis and TOC analyses, the OSI values of the MS samples are found to vary between 22.42 mg/g and 107.58 mg/g, with an average value of 47.21 mg/g. The analyzed FLS samples present OSI values ranging from 40.23 mg/g to 142.67 mg/g (avg. 63.84 mg/g), suggesting relatively favorable oil fluidity. Conversely, the TLS samples exhibit the poorest oil fluidity, with OSI values varying from 18.17 mg/g to 44.38 mg/g (avg. 33.06 mg/g). According to the results from multi-temperature pyrolysis, the ranges of movable oil contents (i.e., $S'_{1\text{-}1}+S'_{1\text{-}2}$) of the MS, FLS and TLS samples are 1.08–4.35 mg/g (avg. 2.79 mg/g), 0.86–4.44 mg/g (avg. 2.66 mg/g), and 1.26–4.94 mg/g (avg. 3.66 mg/g), respectively. Moreover, the percentage of movable oil (i.e., $(S'_{1\text{-}1}+S'_{1\text{-}2})/(S'_{1\text{-}1}+S'_{1\text{-}2}+S'_{2\text{-}1})$) for the tested MS samples ranges from 24.34% to 52.68%, with an average value of 42.11%. The FLS samples present movable oil percentages ranging from 19.18% to 56.87% with an average value of 45.40%. Conversely, the TLS samples present the lowest proportion of mobile oil, with percentages ranging from 26.00% to 45.48% (avg. 31.88%), indicating that the shale oil in the TLS samples predominantly exists in the adsorbed state.

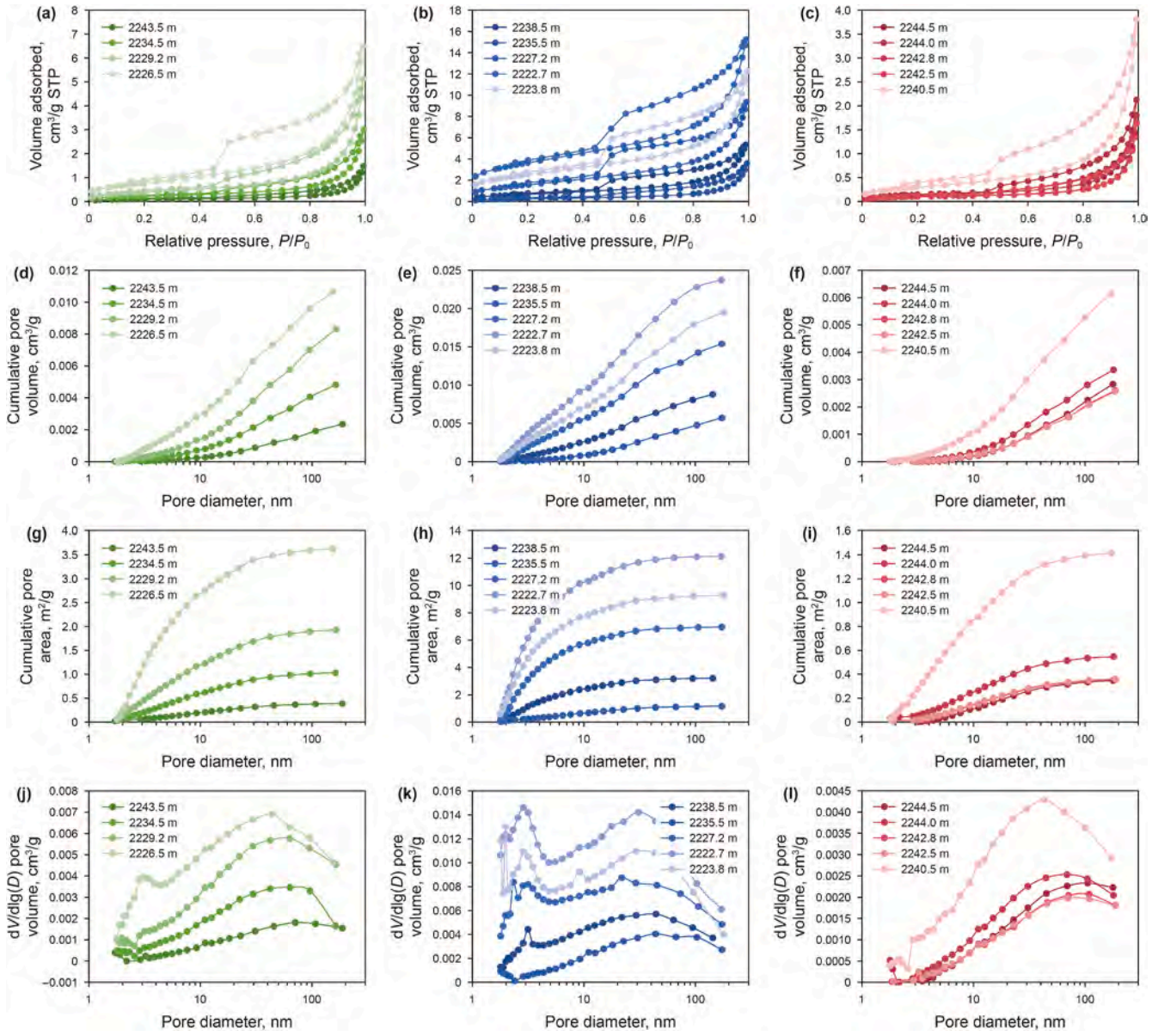

Fig. 6. N_2 adsorption results for the studied shale samples. N_2 adsorption–desorption isotherm curves of the **(a)** MS, **(b)** FLS, and **(c)** TLS samples. Cumulative pore volume versus pore diameter of the **(d)** MS, **(e)** FLS, and **(f)** TLS samples. Cumulative pore area versus pore diameter of the **(g)** MS, **(h)** FLS, and **(i)** TLS samples. Cross-plots of the dV/dlg(D) pore volume–pore diameter for the **(j)** MS, **(k)** FLS, and **(l)** TLS samples in the Chang 7_3 shale. MS = massive shale; FLS = felsic laminated shale; and TLS = tuffaceous laminated shale.

Table 1
Average pore diameter, specific surface area, and total pore volume of the Chang 7_3 shale samples studied by N_2 adsorption.

Shale type	BJH average pore diameter, nm	BET specific surface area, m^2/g	BJH total pore volume, $\times10^{-3}$ cm^3/g
Massive shale (MS)	6.64–14.45 (10.25)	0.33–9.16 (1.49)	1.84–18.12 (6.59)
Felsic laminated shale (FLS)	5.82–12.46 (9.13)	0.95–19.24 (3.64)	5.55–38.00 (10.88)
Tuffaceous laminated shale (TLS)	6.65–14.74 (12.07)	0.35–9.17 (1.64)	2.79–18.10 (5.33)

Note: Minimum–Maximum (Average).

The T_1–T_2 spectra derived from two-dimensional NMR spectroscopy are used to measure the relative quantities of fluids in different occurrence states within the shale, including bound water, free water, adsorbed oil and movable oil. In this study, by systematically comparing the T_1–T_2 spectra of samples in various states (original, dried, water-saturated, oil-saturated, water-saturated centrifuged, and oil-saturated centrifuged), the fluid signals in different occurrence states were separated and identified, thereby establishing a classification chart for the different fluid components. Specifically, movable oil and adsorbed oil were primarily determined by the signal differences between the oil-saturated sample and the oil-saturated centrifuged sample. The signals that decreased after centrifugation of the oil-saturated samples corresponded to the movable oil, while the remaining

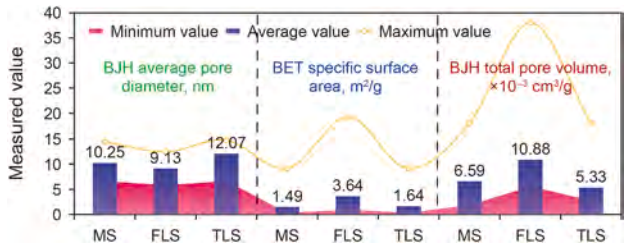

Fig. 7. The bar chart shows the comparison of N_2 adsorption parameters for different types of shale. MS = massive shale; FLS = felsic laminated shale; and TLS = tuffaceous laminated shale.

fluid signals generally corresponded to the adsorbed oil in a strongly bound state. In this way, the distribution ranges of kerogen/solid bitumen ($T_2 < 0.2$ ms, $T_1/T_2 > 100$), adsorbed oil (0.2 ms $< T_2 <$ 1 ms, $T_1/T_2 > 10$), movable oil ($T_2 > 1$ ms, $T_1/T_2 > 10$), bound water ($T_2 < 0.2$ ms, $T_1/T_2 < 100$), and free water ($T_2 > 0.2$ ms, $T_1/T_2 < 10$) in the T_1–T_2 spectra were determined respectively. As illustrated in Fig. 9, the TLS samples exhibit a strong adsorbed oil signal with a small detectable movable oil signal, suggesting overall unfavorable oil fluidity. Although more movable oil signals can be observed in the MS samples, the detectable adsorbed oil signal remains high, suggesting that the shale oil mainly exists in the adsorbed state. Conversely, the FLS samples present the highest detectable movable oil signals and are very close to the adsorbed oil signals, suggesting the most favorable oil fluidity among the three different shale types.

3.5. Chemical composition characteristics of chloroform extracts

Chemical composition analysis of chloroform extracts fractionated from rock samples can offer significant insights into the fluidity of shale oil. Theoretically, the contents of saturate, aromatic, nonhydrocarbon and asphaltene components can represent the individual physical and chemical properties of shale oil. Specifically, shale oil tends to exhibit favorable fluidity when the saturate content is high. With respect to the chloroform extracts obtained from the MS samples, the percentage of saturates varies between 20.49% and 56.33%, with an average value of 41.39% (Fig. 10). Moreover, the average percentages of aromatics, nonhydrocarbons and asphaltenes identified in the MS samples are 26.17%, 27.48%, and 4.946%, respectively. The chloroform extracts from the FLS samples contain saturate hydrocarbons ranging from 31.61% to 59.53% (avg. 46.92%), whereas the average contents of aromatics, nonhydrocarbon and asphaltene are 21.60%, 27.26% and 4.22%, respectively. This finding indicates a relatively favorable fluidity compared with the shale oil present in the MS samples. In terms of the chloroform extracts fractionated from the TLS samples, the detectable saturate hydrocarbon content is determined to be the lowest, and it varies between 22.72% and 34.90%, with an average value of 28.82%. Additionally, the contents of aromatics, nonhydrocarbons and asphaltenes significantly increase, with mean values of 30.79%, 34.02% and 6.365%, respectively, indicating relatively poor fluidity. Overall, the chemical compositions of the TLS, MS, and FLS extracts show gradually increasing saturate hydrocarbon contents, suggesting that the fluidity of the oil improves.

4. Discussion

4.1. Evidence of shale oil migration across the μm–m scale

Determining the occurrence positions of shale oil migration in different source–reservoir units is a key basis for discussing the mobility effects of migration differentiation. However, due to the short migration distance and multiscale nature, accurately

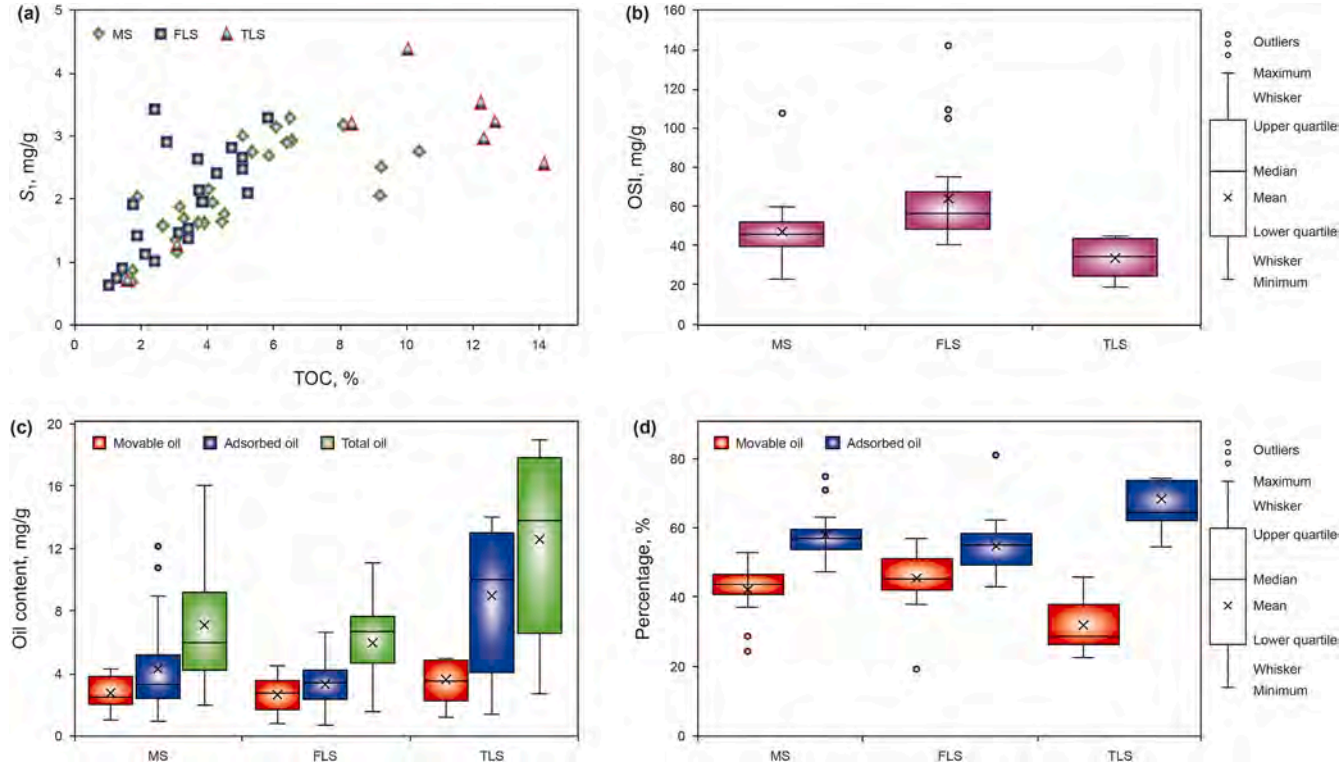

Fig. 8. Rock–Eval pyrolysis and multi-temperature pyrolysis results for the studied Chang 7_3 shale samples. **(a)** Cross-plot of the S_1–TOC for the MS, FLS, and TLS samples. **(b)** OSI box plots for the MS, FLS, and TLS samples. **(c)** Box plot showing the distribution of the oil content for the MS, FLS, and TLS samples. **(d)** Box plot illustrating the adsorbed and movable oil percentages for the MS, FLS, and TLS samples. MS = massive shale; FLS = felsic laminated shale; and TLS = tuffaceous laminated shale.

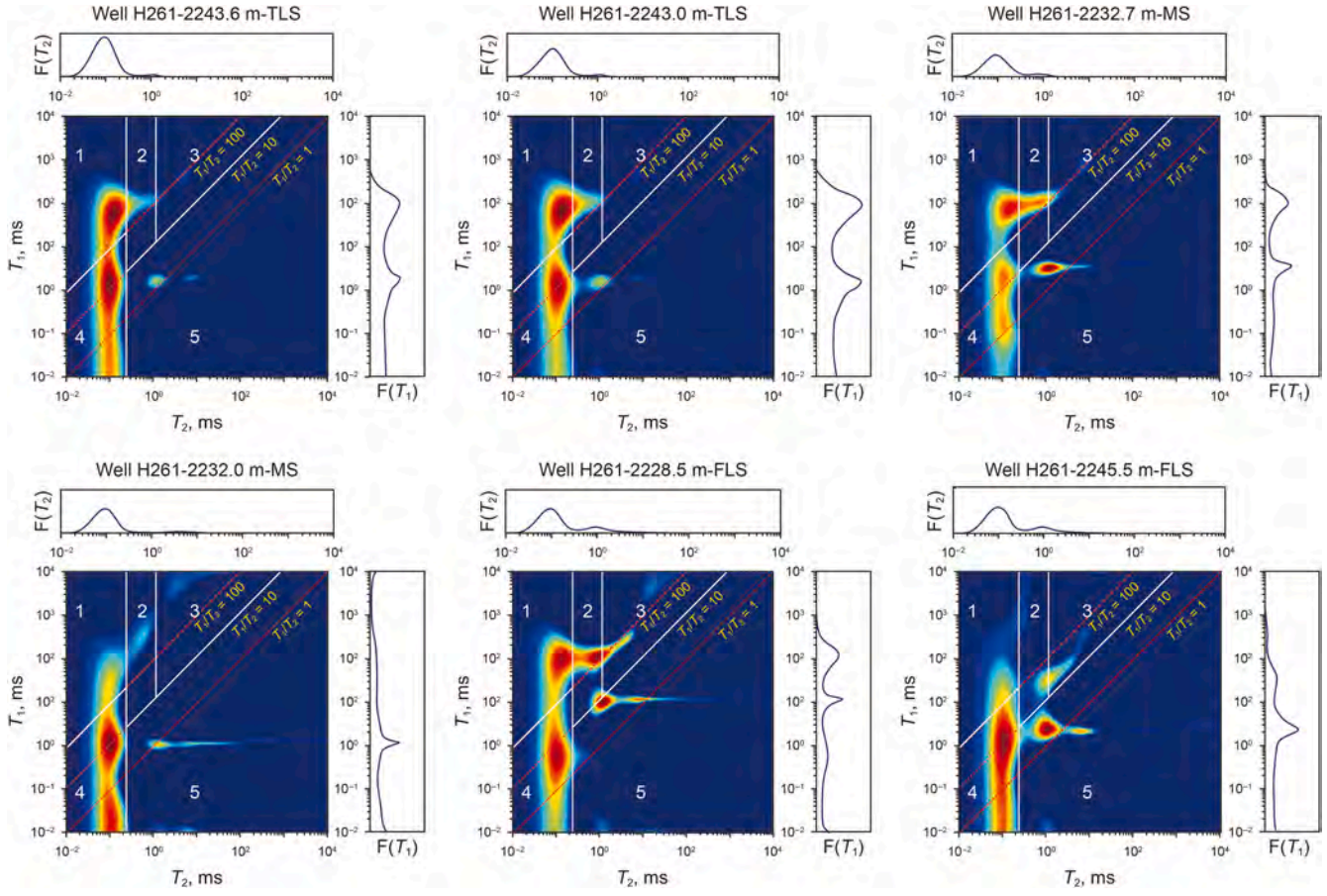

Fig. 9. NMR results for typical shale samples from the Chang 7_3 lacustrine shale. Regions 1 to 5 represent kerogen/solid bitumen (T_2 < 0.2 ms, T_1/T_2 > 100), adsorbed oil (0.2 ms < T_2 < 1 ms, T_1/T_2 > 10), movable oil (T_2 > 1 ms, T_1/T_2 > 10), bound water (T_2 < 0.2 ms, T_1/T_2 < 100), and free water (T_2 > 0.2 ms, T_1/T_2 < 10), respectively.

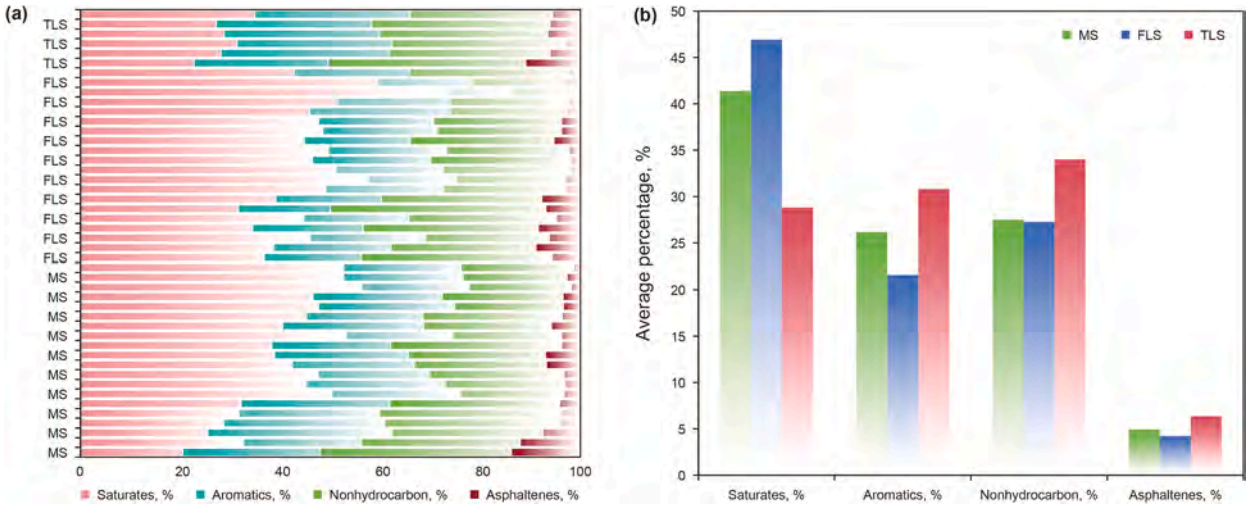

Fig. 10. **(a)** Relative contents and **(b)** average contents of different chemical compositions of extracts from the Chang 7_3 lacustrine shale samples.

implementing shale oil migration tracing through a single geochemical index or method faces challenges. To this end, this study combined LSCM, pyrolysis parameter anomalies, original–true hydrocarbon generation potential differences, chemical composition differentiation, and n-alkane differentiation to comprehensively identify and discuss multiscale shale oil migration phenomena.

4.1.1. Interlaminar shale oil migration at the μm–mm scale

High-resolution LSCM can be utilized to effectively analyze the occurrence and migration differentiation characteristics of shale oil components in the micrometer–sub-micrometer pores of typical shale samples (Gao et al., 2023). Specifically, the function of LSCM in receiving fluorescence signals of different bands can be utilized to qualitatively and quantitatively evaluate the

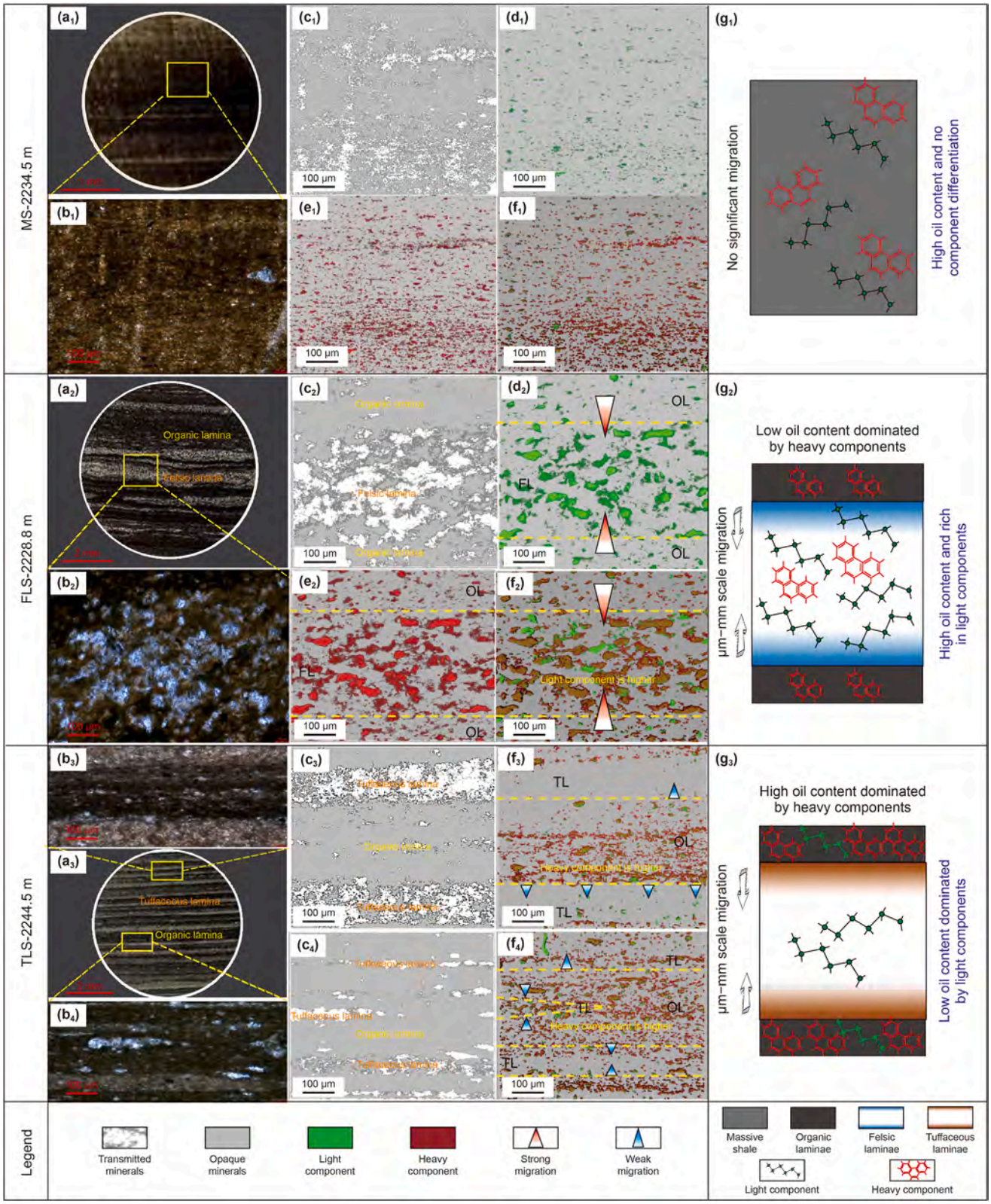

Fig. 11. Occurrence characteristics of light/heavy oil components in typical shale samples under LSCM. **(a)**, **(b)** and **(c)** show massive/laminated shale under plane-polarized light, orthogonal light and transmitted light, respectively. **(d)** Distribution of the oil light component (green color). **(e)** Distribution of heavy components (red color). **(f)** Light–heavy component superposed plots. OL = organic laminae; FL = felsic laminae; and TL = tuffaceous laminae. **(g)** Conceptual diagram illustrating the interlaminar light/heavy component differentiation in the shale.

Table 2
Quantitative results of light and heavy components of different shale types and internal laminae.

Sample depth, m	Shale type		Measuring position	Light component volume percentage, %	Heavy component volume percentage, %	Light/heavy component ratio
2234.5	MS		Fig. 11(f_1)	3.623	7.376	0.491
2228.8	FLS	OL	Fig. 11(f_2)	1.956	6.298	0.311
		FL		8.824	14.695	0.600
2244.5	TLS	OL	Fig. 11(f_3)	3.082	6.428	0.479
		TL		0.745	1.134	0.657
	TLS	OL	Fig. 11(f_4)	4.882	9.155	0.533
		TL		1.601	2.289	0.699

Note: MS = massive shale; FLS = felsic laminated shale; TLS = tuffaceous laminated shale; OL = organic laminae; FL = felsic laminae; and TL = tuffaceous laminae.

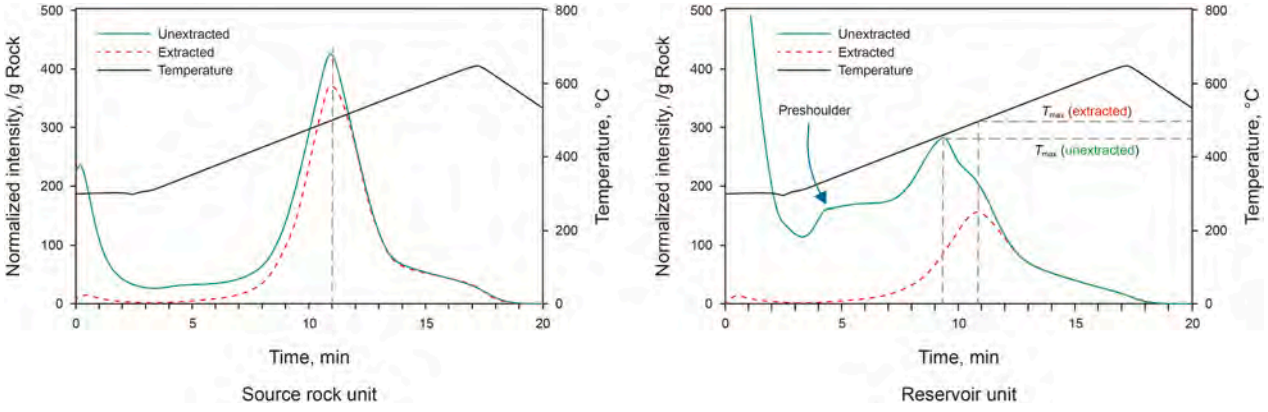

Fig. 12. Rock–Eval curves of the Chang 7 shale before (green solid lines) and after (red dashed lines) the Soxhlet extraction as a function of time (Zou et al., 2019).

distribution and content of light and heavy components (including heavy oil, gelatinous asphaltenes, etc.) in shale oil. In this way, based on the geochromatography effect during the petroleum migration process, the migration phenomenon of shale oil at the μm–mm scale can be analyzed, especially between different laminae.

In this study, disparities in hydrocarbon generation and storage capacity between different laminae provide favorable conditions for interlaminar shale oil migration, which is proven by detectable oil composition differentiation at the μm–mm scale according to LSCM (Fig. 11; Table 2). Theoretically, organic laminae (OLs) are considered oil-generating units because of their strong hydrocarbon generation/expulsion capacity, whereas organic-poor felsic laminae (FLs) and tuffaceous laminae (TLs) are generally considered reservoir units. In general, according to geochromatography in petroleum migration, migrating hydrocarbons are chemically lighter than retained hydrocarbons because of their good mobility (Charlesworth, 1986; Brother et al., 1991; Bennett et al., 2002; Ataman et al., 2016), thus contributing to the enrichment of light components in the reservoir unit. For MS, the absence of overlapping laminated structures leads to no distinct source–reservoir unit within the shale, where the light components (green color) and heavy components (red color) detected via LSCM exhibit a random dispersion distribution and no significant component differentiation (Fig. 11(a_1)–(g_1)). The light/heavy component ratio of the MS sample quantitatively detected was 0.491. It is evident that the μm–mm-scale shale oil migration phenomenon is not widespread within the MS. Regarding the FLS, significant oil composition differentiation can be observed in the microscopic source–reservoir unit composed of organic matter and felsic laminates. As illustrated in Fig. 11(d_2)–(f_2), the detectable residual oil content in the OL is generally low (volume percentage is 8.254%) and is predominantly composed of heavy components (volume percentage is 6.298%), suggesting that most of the light hydrocarbons have migrated away. Correspondingly, the FL adjacent to the OL has a high oil content (volume percentage is 23.519%) and is relatively rich in light hydrocarbon components (volume percentage is 8.824%) compared to OL, indicating significant oil content variations and oil component differentiation caused by the migration of hydrocarbon inputs (Fig. 11(g_2)). The light/heavy component ratios for OL and FL were 0.311 and 0.600, respectively. This apparent disparity in light/heavy component ratio can be attributed to the favorable reservoir capacity of FL facilitating oil migration. Unlike FLS, the detectable oil content within TLS is enriched in OL rather than in TL, and it is composed mainly of heavy components (Fig. 11(f_3) and (f_4)). As shown in Fig. 11(f_3), the detectable oil volume percentage and the light/heavy component ratio of OL are 9.510% and 0.479 respectively, implying a large amount of crude oil retention. Owing to the low total pore volume, which is not conducive to hydrocarbon charging and migration, the TL is characterized by a low oil content (volume percentage is 1.890%) and a higher light/heavy component ratio (0.657). Similar features are also shown in Fig. 11(f_4). This component differentiation also confirms the occurrence of oil migration between OL and TL (Fig. 11(g_3)). According to the detectable oil content and light/heavy component ratio disparity of different laminae, shale oil migration in the OL–FL laminae assemblage is evidently easier and stronger than that in the OL–TL laminae assemblage. Overall, laminated shales are more prone to obvious μm–mm-scale shale oil migration than massive shales are, and FLSs exhibit more significant interlaminar shale oil migration than TLSs do.

4.1.2. Shale oil migration across the laminae assemblage at the cm–m scale

The cm–m-scale oil migrations across the laminae assemblage (or lithofacies) can also be observed in the Chang 7_3 shale, which is distinguished by the following four aspects: pyrolysis parameter

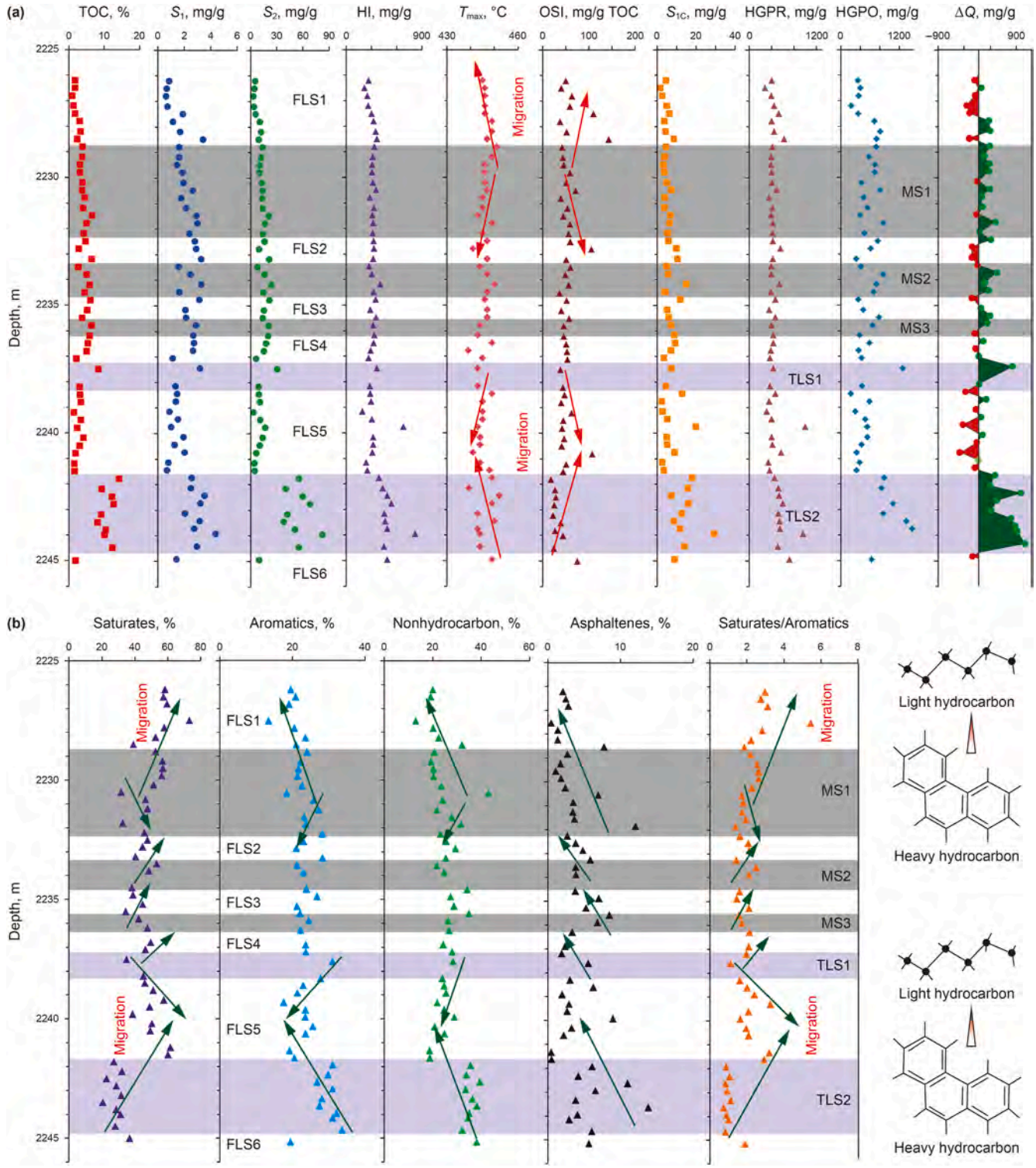

Fig. 13. Geochemical profiles of the Chang 7_3 shale in Well H-261. **(a)** Vertical variation in the TOC content, Rock–Eval pyrolysis parameters, and ΔQ (HGPO − HGPR). **(b)** Vertical chemical composition differentiation of chloroform extracts. FLS1 to FLS6 represent major felsic laminated shale units. MS1 and MS2 are the main massive shale units. TLS1 and TLS2 indicate tuffaceous laminated shale units.

anomalies, original–true hydrocarbon generation potential differences, chemical composition differentiation, and n-alkane differentiation.

Firstly, the presence of migrated hydrocarbons can be identified by using the Rock–Eval pyrolysis spectra before and after extraction. Many scholars have found that the input of migrated hydrocarbons can cause a preshoulder before the peak of pyrolysis hydrocarbons (S_2), which is due to the mixture of heavy oil or asphalt in the migrated hydrocarbon and products within the S_2 peak temperature range, thus represses the S_2 peak temperature, that is, reducing the maximum pyrolysis peak temperature (T_{max}) value (Han et al., 2015, 2019; Li et al., 2018; Zou et al., 2019). As

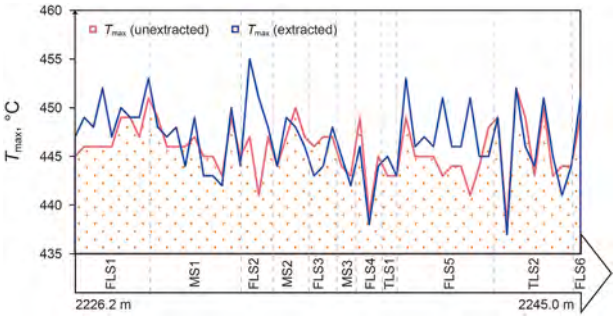

Fig. 14. Comparison of T_{max} values before and after extraction in different shale units of Chang 7_3 shale in the study area.

shown in Fig. 12, existing studies have revealed that there is no significant change in the T_{max} value corresponding to the S_2 peak of the source rock unit samples before and after extraction. However, for the reservoir unit samples before extraction, there was a distinct preshoulder before the S_2 peak and it exhibits a relatively low T_{max} value. After solvent extraction, the peak value of S_2 was significantly lower compared to the source rock unit (Fig. 12(a)), while the corresponding T_{max} value was larger than that of the reservoir unit samples before extraction (Fig. 12(b)). This phenomenon also exists in the Barnett shale and the Niobrara shale (Han et al., 2015, 2019). The peak value and curve shape of free hydrocarbons (S_1) and S_2 reflect the source of hydrocarbons, so whether they are affected by external hydrocarbons can be evaluated by comparing the pyrolysis images of samples with similar maturity (Li et al., 2018). Moreover, shale samples stained by migrated hydrocarbons usually have the characteristics of low organic carbon mass (TOC), low S_2, high productivity value (PI), and high oil saturation value (OSI) (Li et al., 2018; Han et al., 2019; Ma et al., 2019; Hackley et al., 2020; Guo et al., 2022), indicating that this type of shale has a relatively low hydrocarbon generation potential, but the free hydrocarbons have relatively high values. In summary, the input of migrating hydrocarbons tends to increase the free oil content and inhibits T_{max}, resulting in the typical characteristics of low TOC, low S_2, high S_1, high OSI, and low T_{max} in the shale units that received migrating hydrocarbons (Gao et al., 2024; Hu et al., 2024a, 2024b). In this study, the OSI (or S_1/TOC) and T_{max} anomalies were employed to identify the nonprimary hydrocarbons caused by shale oil migration. According to the laminae type and assemblage characteristics, the Chang 7_3 shale in Well H-261 can be approximately divided into 6 FLS units, 2 MS units and 2 TLS units. As illustrated in Fig. 13(a), the FLS1, FLS2, and FLS5 units present abnormally high OSIs and abnormally low T_{max} values relative to those of the adjacent MS and TLS units, suggesting that shale oil may migrate across the laminae assemblage from the MS/TLS unit to the FLS unit. Moreover, the T_{max} differences of the FLS1, FLS2 and FLS5 unit samples before and after extraction (Fig. 14), that is, the unextracted T_{max} value is significantly smaller than the extracted T_{max} value, also suggest the possible input of migrated hydrocarbons. However, no significant pyrolysis parameter anomalies can be detected between the FLS3 and FLS4 units and the adjacent MS and TLS units, which implies that in the thin interbedded and geologically similar source–reservoir assemblage, oil migration across the laminae assemblage may be too small in scale or limited in quantity to cause obvious changes in the pyrolysis parameters.

In addition to these pyrolysis parameter anomalies, some scholars have calculated the original hydrocarbon generation potential and current true hydrocarbon generation potential of different units in shale through the mass balance principle, and then evaluated the content of migrated hydrocarbon by the difference between these two values (Hu et al., 2024a, 2024b). According to the mass balance principle, geochemical data from Rock–Eval/TOC analysis can be employed to quantify the original hydrocarbon generation potential (HGPO) and the current true hydrocarbon generation potential (HGPR). The key steps for restoring HGPO involve determining the kerogen conversion rates of different shale samples. However, the highly heterogeneous nature of lacustrine shale makes the hydrocarbon generation reaction pathways of different kerogen types vary widely, which brings uncertainty to the determination of conversion rates. To obtain a more accurate hydrocarbon conversion process, this study first classified the organic matter types of specific samples and simulated the hydrocarbon generation kinetic reaction paths of different kerogens (i.e., type I, II_1, II_2, and III) during the thermal maturation process. Subsequently, based on the organic matter types of specific samples, the corresponding hydrocarbon generation evolution models were selected to calculate the HI values under different maturity levels. Finally, the calculated HI values and the fitted original HI values of different kerogens were combined to determine the kerogen conversion rate. Once the HGPO values were restored based on the kerogen conversion rate, ΔQ (HGPO − HGPR) can be utilized to achieve a quantitative assessment of shale oil migration (for detailed information, refer to Hu et al. (2024a)). $\Delta Q<0$ represents the external hydrocarbon content received by the shale as a reservoir unit, while $\Delta Q>0$ indicates the amount of hydrocarbons expelled by the shale as a source rock unit. In the Chang 7_3 shale system, the MS and TLS units collectively behave as oil-generating units because they exhibit the typical characteristics of $\Delta Q>0$, whereas FLSs generally behave as reservoir units with $\Delta Q<0$ (Fig. 13(a)). The FLS1, FLS2 and FLS5 units receive more external migrating hydrocarbons ($\Delta Q<-200$ mg/g), while the FLS3 and FLS4 units exhibit weaker oil migration because migratory hydrocarbons are generally less than 50 mg/g. Moreover, some evaluated samples are confirmed to have ΔQ values greater than 0.

On the other hand, the fractionation of hydrocarbon components during petroleum migration has been successfully simulated in the laboratory, and this phenomenon is also manifested in shale oil migration (Han et al., 2015; Zou et al., 2019). From a chemical perspective, saturate hydrocarbons and aromatic hydrocarbons are preferentially discharged compared to non-hydrocarbons and asphaltenes (Jarvie, 2014), tending to result in a richer polar component in the source rock unit and a richer non-polar component in the reservoir unit. Similarly, physical fractionation also exists during oil migration, that is, small-molecule compounds are more likely to be discharged from the source unit (Jarvie, 2014). The sections with external hydrocarbons have the typical feature of a relatively low content of multi-carbon number normal alkanes, while the content of low-carbon number normal alkanes is significantly high (Dai et al., 2021). Therefore, the compositional fractionation of chloroform extracts derived from shale samples can provide significant insights into shale oil migration at the cm–m scale.

The chemical composition variation in the shale oil within the different source–reservoir units of the Chang 7_3 shale can be detected (Fig. 13(b)). For the TLS1–FLS5–TLS2 configuration unit, shale oil migration across the laminae assemblage from the TLS to the FLS can be clearly observed, which manifests as a gradual increase in the saturate hydrocarbon content and saturation/aromatics ratio in the migration direction. Conversely, the nonhydrocarbon and asphaltene contents decrease significantly in the migration direction. In the FLS1–MS1 configuration unit, shale oil migration from MS to FLS can be clearly observed, which is reflected by the gradually increasing saturate hydrocarbon content and saturation/aromatics ratio and the

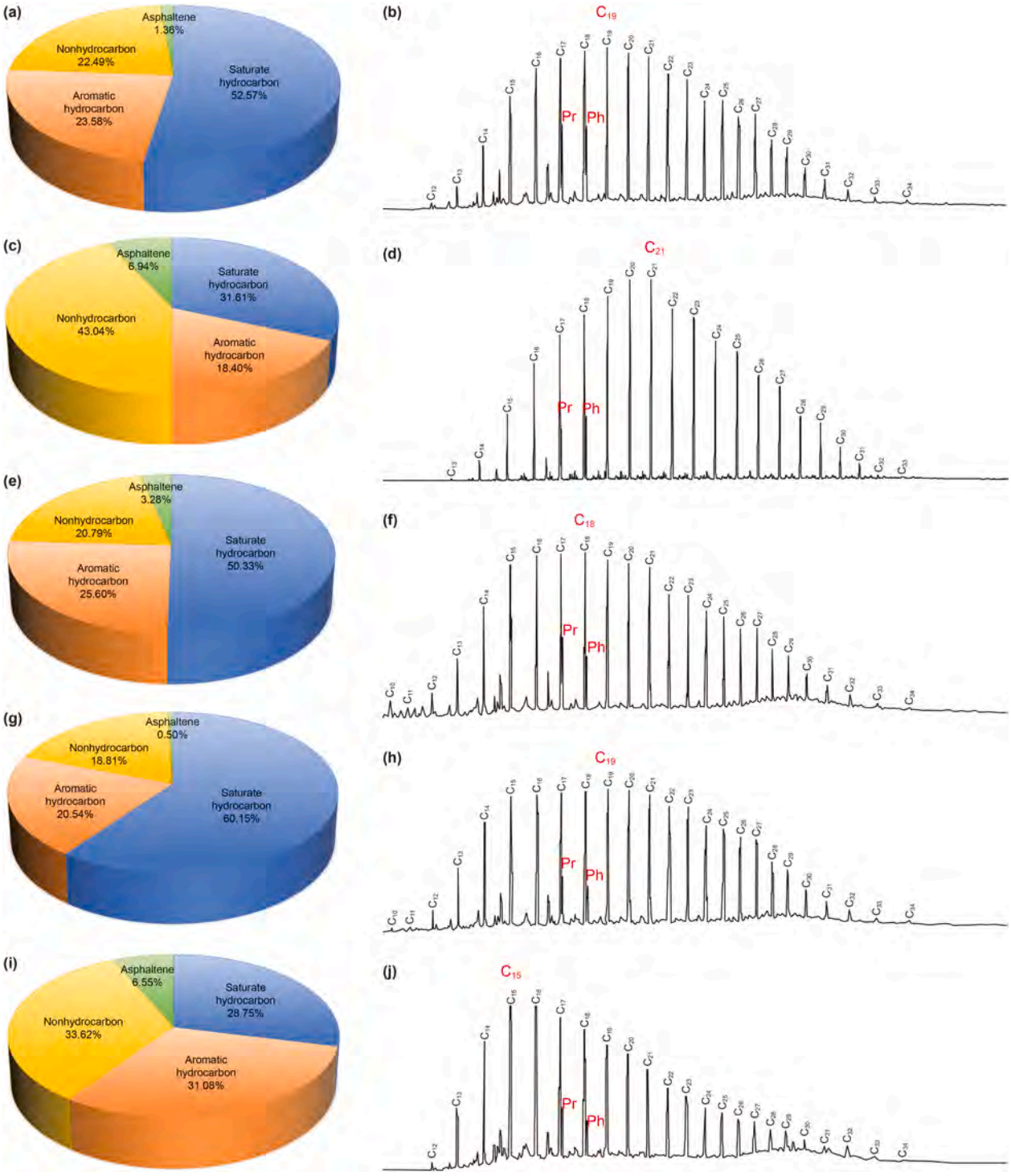

Fig. 15. Chemical compositions and typical *m/z* 85 mass chromatographic characteristics of chloroform extracts from typical shale samples. **(a)** Chemical composition contents and **(b)** mass chromatograms of shale oil from the FLS1 unit in Well H-261 (2227.8 m). **(c)** Chemical composition contents and **(d)** mass chromatograms of shale oil from the MS1 unit in Well H-261 (2230.5 m). **(e)** Chemical composition contents and **(f)** mass chromatograms of shale oil from the FLS5 unit in Well H-261 (2240.2 m). **(g)** Chemical composition contents and **(h)** mass chromatograms of shale oil from the FLS5 unit in Well H-261 (2241.5 m). **(i)** Chemical composition contents and **(j)** mass chromatograms of shale oil from the TLS2 unit in Well H-261 (2242.8 m).

decreasing nonhydrocarbon and asphaltene content in the migration direction. Consequently, the saturate hydrocarbon contents detected in the FLS1 and FLS5 units are significantly greater than those detected in the adjacent MS and TLS units (Fig. 15). Notably, detectable compositional differentiation in the FLS2–MS2–FLS3–MS3–FLS4–TLS1 configuration unit is relatively weak because the thin layer thickness limits the possible maximum migration distance of shale oil.

Furthermore, biomarker compounds are effective indicators of hydrocarbon migration (Fan and Philp, 1987; Sivan et al., 2008),

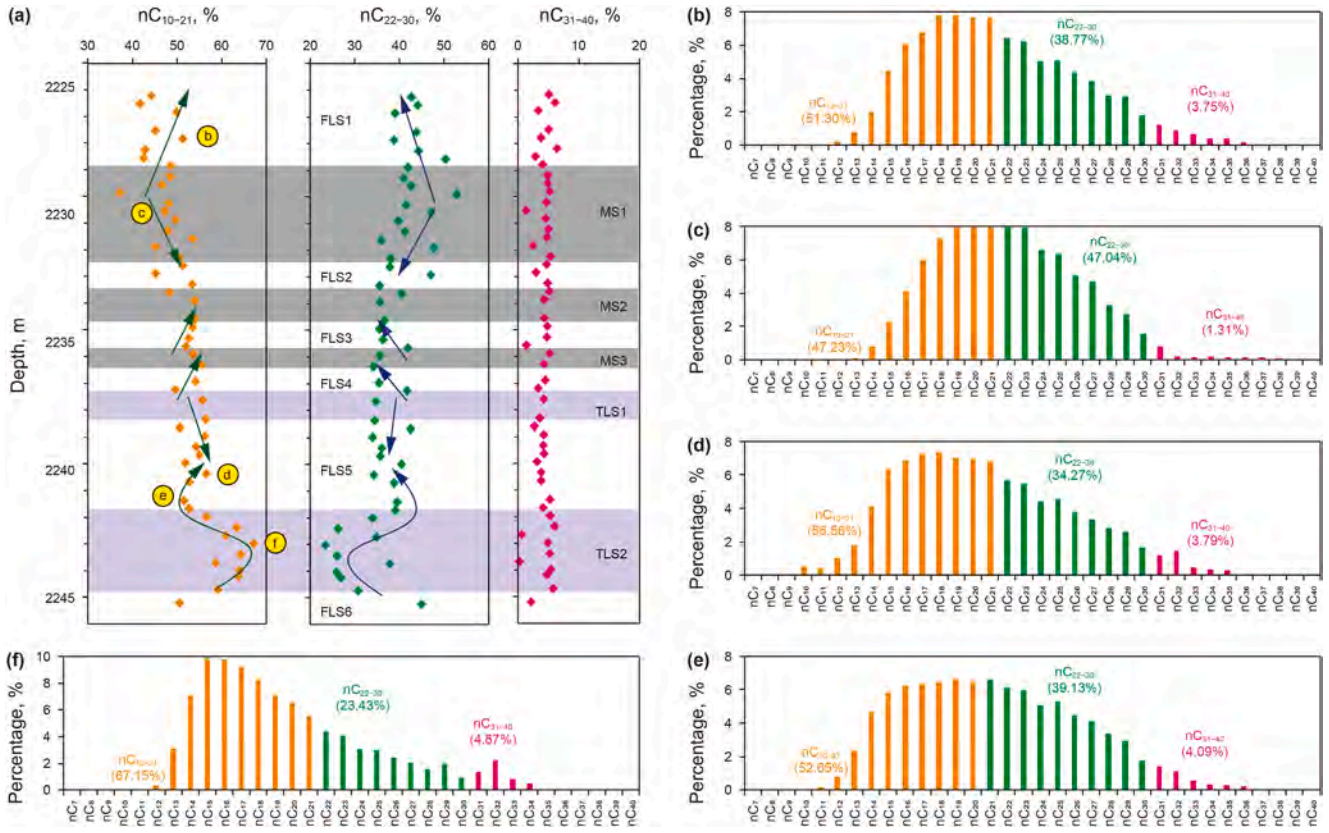

Fig. 16. n-Alkanes with different carbon contents in typical shale samples. **(a)** Profile showing the variations in n-alkanes in Well H-261. **(b)** n-Alkane compound of shale oil from the FLS1 unit in Well H-261 (2227.8 m). **(c)** n-Alkane compound of shale oil from the MS1 unit in Well H-261 (2230.5 m). **(d)** n-Alkane compound of shale oil from the FLS5 unit in Well H-261 (2240.2 m). **(e)** n-Alkane compound of shale oil from the FLS5 unit in Well H-261 (2241.5 m). **(f)** n-Alkane compound of shale oil from the TLS2 unit in Well H-261 (2242.8 m).

among which n-alkanes can be utilized to trace shale oil migration because of their ability to indicate the nature of light/heavy hydrocarbon properties (Leythaeuser et al., 1979; Burruss and Hatch, 1989). Statistical results for the n-alkanes (the n-alkanes with carbon numbers of 10–21 ($nC_{10–21}$), 22–30 ($nC_{22–30}$) and 30–40 ($nC_{30–40}$) are counted separately) confirm the migration differentiation within different source–reservoir units (Fig. 16). Specifically, an increase in the $nC_{10–21}$ content and a decrease in the $nC_{22–30}$ content can be observed in the migration direction. Nevertheless, there is no discernible variation in the $nC_{30–40}$ content (Fig. 16(a)–(e)). Notably, despite the low level of saturate hydrocarbon content in the TLS2 unit (Fig. 15(i)), an abnormally high level of $nC_{10–21}$ can be detected in the middle section (Figs. 15(j) and 16(f)). This anomaly is speculated to be related to the pore structure of TLSs. The adverse pore structure and small pore volume make it challenging for macromolecular compounds (e.g., long-chain n-alkanes) to enter the small pore throats of TLSs, resulting in the relative enrichment of small-molecule compounds (e.g., short-chain n-alkanes). Moreover, the unfavorable pore structure and thick organic-rich shale can effectively prevent hydrocarbon expulsion and light hydrocarbon escape, which tends to be an additional reason for the high concentration of short-chain n-alkanes in the midsection of the TLS.

In summary, on the basis of multi-type hydrocarbon migration evaluation and tracking, significant cm–m-scale oil migration across the laminae assemblage (or lithofacies) can be detected in the thick MS/TLS (i.e., source rock unit) and thick FLS (i.e., reservoir unit) configurations. However, this shale oil migration phenomenon is not widespread in the thin MS/TLS (i.e., source rock unit) or thin FLS (i.e., reservoir unit) configurations.

4.2. Effects of migration differentiation on shale oil mobility

4.2.1. Control of external hydrocarbon migration on oil composition and mobility

From the perspective of hydrocarbon migration physics, light and low-polarity components (e.g., saturate hydrocarbons) exhibit higher flow capacity and migration efficiency in porous media due to their simple molecular structure, weak intermolecular forces, and low viscosity (Charlesworth, 1986; Brother et al., 1991). Therefore, during the process of migrated hydrocarbon charging into shale reservoir units, a significant migration differentiation effect occurs, that is, these light components such as saturate hydrocarbons are preferentially displaced and migrated, while the heavier components with stronger polarity and more complex molecular structures, such as aromatic hydrocarbons, NSO compounds, and asphaltenes, are more easily adsorbed and retained in the migration path or source rock units (Bennett et al., 2002; Ataman et al., 2016). Once these highly mobile migrated hydrocarbons enter the reservoir units, they will directly dilute the original hydrocarbon composition and increase the proportion of light components. Simultaneously, competitive adsorption of hydrocarbons on the surface of minerals and organic matter will also occur (Hong et al., 2022). Specifically, the increase of saturate hydrocarbons with adsorption capacity far weaker than that of polar components will significantly reduce the adsorbed oil

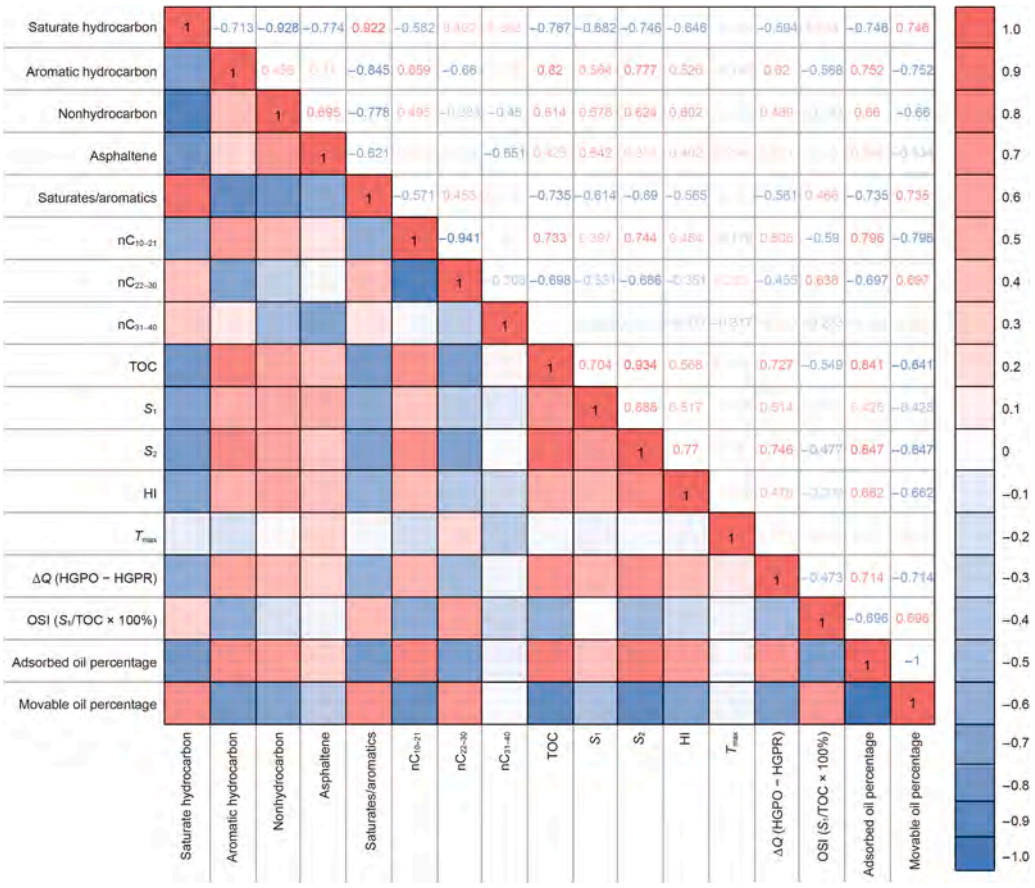

Fig. 17. Pearson correlation heatmap showing the relationships among the chemical composition, pyrolysis parameters, migration hydrocarbon (ΔQ) and mobility indices of the shale oil.

content of the entire reservoir unit, and instead increase the proportion of free and movable oil, thereby fundamentally improving the fluidity and mobility of shale oil. In this study, the pore structure also has a significant impact on the competitive adsorption and migration differentiation of shale oil. For FLS, which serves as the main reservoir unit, the characteristics of high specific surface area (avg. 3.64 m^2/g) and small pore diameters (avg. 9.13 nm) enable strong adsorption and retention of heavy polar components at the oil injection front, thereby causing the molecular sieve effect in the migrating hydrocarbon flow. This process tends to make the hydrocarbon components that can penetrate the reservoir significantly lighter. Moreover, the high total pore volume (avg. 10.88×10^{-3} cm^3/g) of FLS typically features sufficient storage space for the input migrating hydrocarbons, enabling the relative enrichment of free-phase oil dominated by low-viscosity saturate hydrocarbons, thereby improving the fluidity of the shale oil.

To precisely assess the association between imported externally migrating hydrocarbons and shale oil mobility, we conducted a Pearson correlation heatmap analysis, and the results are shown in Fig. 17. The oil saturation index (OSI) and movable oil percentage are positively correlated with the parameters related to the saturate hydrocarbon composition, including the saturate content, saturate/aromatic ratio, and $nC_{22–30}$. The mobility of shale oil is closely related to the content of light components, especially saturate hydrocarbons. Conversely, the OSI and movable oil percentage are negatively correlated with aromatic hydrocarbons, nonhydrocarbons, asphaltene content, $nC_{22–30}$, $nC_{31–40}$, TOC, S_2, and ΔQ (HGPO − HGPR). This result proves that organic geochemical characteristics (e.g., TOC, S_2, and HI), which determine the fundamental basis of hydrocarbon production, can be considered a factor affecting oil mobility. Notably, the abnormal negative correlation between $nC_{22–30}$ and shale oil mobility in this study may be attributed to the enrichment of $nC_{22–30}$ in thick TLSs with unfavorable pore structures. Additionally, because a smaller ΔQ implies more external migration hydrocarbons in the case of $\Delta Q<0$, the negative correlation between ΔQ and shale oil mobility here actually indicates a positive correlation between migration hydrocarbon input and mobility. In essence, the effect of migration differentiation on shale oil mobility manifests as the variation in oil composition and free or movable oil quantity caused by internal migration within shale. This finding can be supported by the overall good correlation between ΔQ, the compositional parameters and the mobility indicators shown in Fig. 17. Thus, we perform a sensitivity analysis between migrating hydrocarbons (reflected by ΔQ), oil chemical compositions (represented by saturate hydrocarbons), and mobility indices (represented by OSI and movable and adsorbed oil percentages) to elucidate this relationship.

As illustrated in Fig. 18(a), a significant negative correlation can be detected between ΔQ and saturate hydrocarbon content, where TLS and MS primarily act as hydrocarbon expulsion units ($\Delta Q>0$). FLS mostly behaves as reservoir units that receive external migrating hydrocarbons ($\Delta Q<0$). This phenomenon implies that the input of good-mobility migrating hydrocarbons directly contributes to the increase in saturate hydrocarbon quantity,

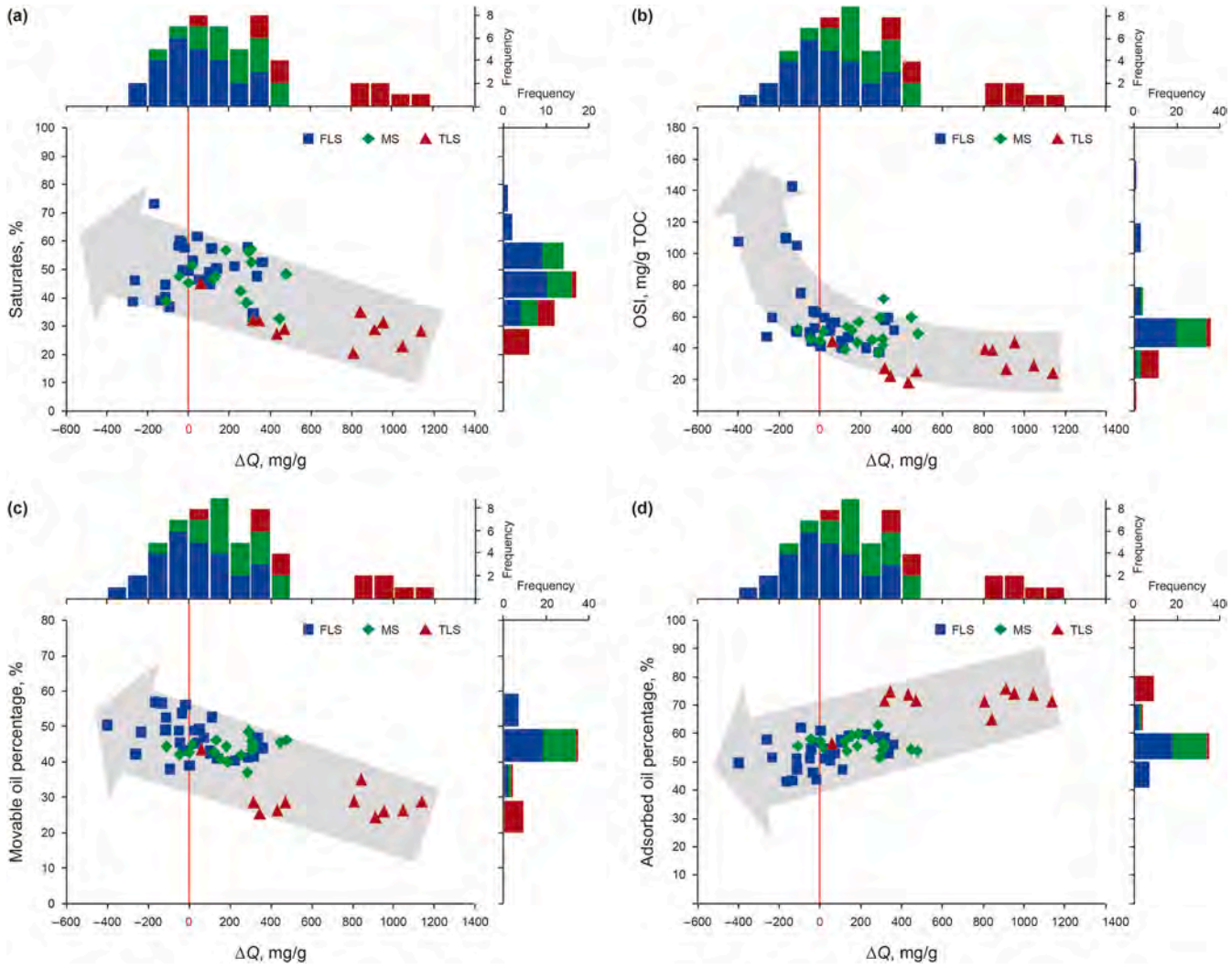

Fig. 18. Cross-plot of ΔQ versus **(a)** saturate, **(b)** OSI, **(c)** movable oil percentage, and **(d)** adsorbed oil percentage. ΔQ = HGPO − HGPR; HGPO = original hydrocarbon generation potential; HGPR = true hydrocarbon generation potential; MS = massive shale; FLS = felsic laminated shale; and TLS = tuffaceous laminated shale.

consequently leading to a generally high saturate hydrocarbon content in FLS. Notably, the OSI is negatively correlated with ΔQ and highly sensitive to the input of migrating hydrocarbons, which is represented by a steep increase in OSI values over the ΔQ<0 interval (Fig. 18(b)). As a result, TLSs and MSs are characterized by low OSI values due to hydrocarbon expulsion, whereas FLSs exhibit high OSI values because they receive large amounts of migrating hydrocarbons. Similarly, an overall negative correlation can be detected between ΔQ and the movable oil percentage, indicating that FLS units with ΔQ<0 have high movable oil percentages and that MS and TLS units with ΔQ>0 have low movable oil percentages (Fig. 18(c)). Conversely, the adsorbed oil percentage is entirely different and positively correlated with ΔQ (Fig. 18(d)). In terms of the effect of chemical composition on shale oil mobility, the detectable saturate content in the chloroform extract is significantly positively correlated with the OSI and movable oil percentage, whereas the adsorbed oil percentage is significantly negatively correlated with the saturate content (Fig. 19). Notably, the OSI and movable oil percentage are typically low and increase very slowly when the saturate content is less than 40%. Conversely, the OSI and movable oil percentage start to rise quickly when the saturate content is near 40% and then remain at a stable high level when the saturate content exceeds 40%. Therefore, a saturate hydrocarbon content of 40% tends to be a critical condition where the mobility of Chang 7_3 shale oil changes significantly from a disadvantageous situation to a favorable situation.

Overall, the variations in oil composition and movable oil content caused by the input of external hydrocarbons along the migration direction are conducive to improving shale oil mobility, especially for reservoir units that receive external hydrocarbons.

4.2.2. Migration differentiation and mobility effects under different source–reservoir configurations

The degree of shale oil migration differentiation is essentially controlled by the seepage conduits and dynamic-resistance conditions formed by the source–reservoir configuration. Theoretically, in a favorable configuration characterized by significant source–reservoir quality gap and the presence of high-permeability conduits, sufficient driving forces and connected pore-fracture networks provide favorable migration conditions for light components, enabling them to be rapidly and continuously discharged from the source rock unit (Guo et al., 2022; Gao et al., 2024; Zhang et al., 2024). This leads to a strong migration differentiation, that is, a significant depletion of light components in the

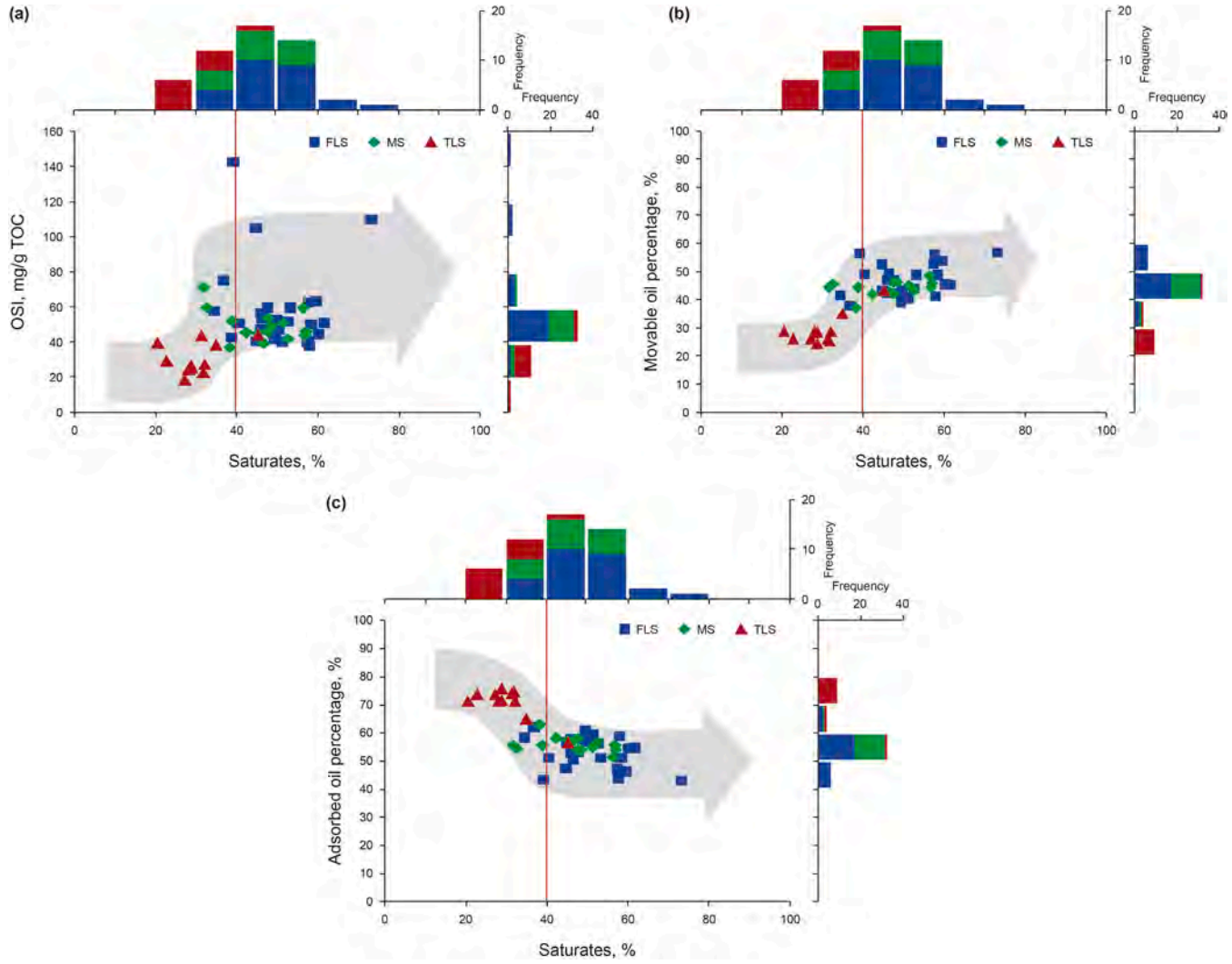

Fig. 19. Cross-plot exhibiting saturates versus **(a)** OSI, **(b)** movable oil percentage, and **(c)** adsorbed oil percentage. MS = massive shale; FLS = felsic laminated shale; and TLS = tuffaceous laminated shale.

source rock units and a significant enrichment in the reservoir units. Conversely, in an unfavorable configuration where the source–reservoir quality is close and the migration path tends to be blocked, hydrocarbons are difficult to be effectively discharged from the source rock unit. Even if shale oil migration occurs, the differentiation effect is relatively weak. The detectable mobility differences of shale oil between the source unit and reservoir unit are largely influenced by the migration differentiation degree under different source–reservoir configurations (Fig. 20). In most cases, when there is no detectable hydrocarbon exchange caused by oil migration, shale oil mobility is generally dependent on the primary oil composition and initial geological features, regardless of the source unit, which has a high oil-generating capacity, or the reservoir unit, which has a high oil storage capacity. However, once shale oil migration occurs under suitable conditions, this process is inevitably accompanied by the loss of light hydrocarbon components in the source unit that expels hydrocarbons and the enrichment of light hydrocarbon components in the reservoir unit that receives external hydrocarbons. Predictably, with increasing migration differentiation intensity, the mobility of the shale oil within the source unit gradually decreases because of the retention of heavy components, whereas the reservoir unit consequently displays greater mobility because of the large-scale input of light components. The mobility difference between source–reservoir units is clearly positively correlated with the intensity of migration differentiation.

This insight can be supported by the shale oil migration differentiation and mobility characteristics within different source–reservoir configurations of the Chang 7_3 shale (Figs. 11 and 21). In terms of interlaminar migration at the μm–mm scale, the OL–FL configurations characterized by a good source–good reservoir exhibit stronger migration differentiation than the OL–TL configurations characterized by a good source–poor reservoir, resulting in the relative enrichment of light

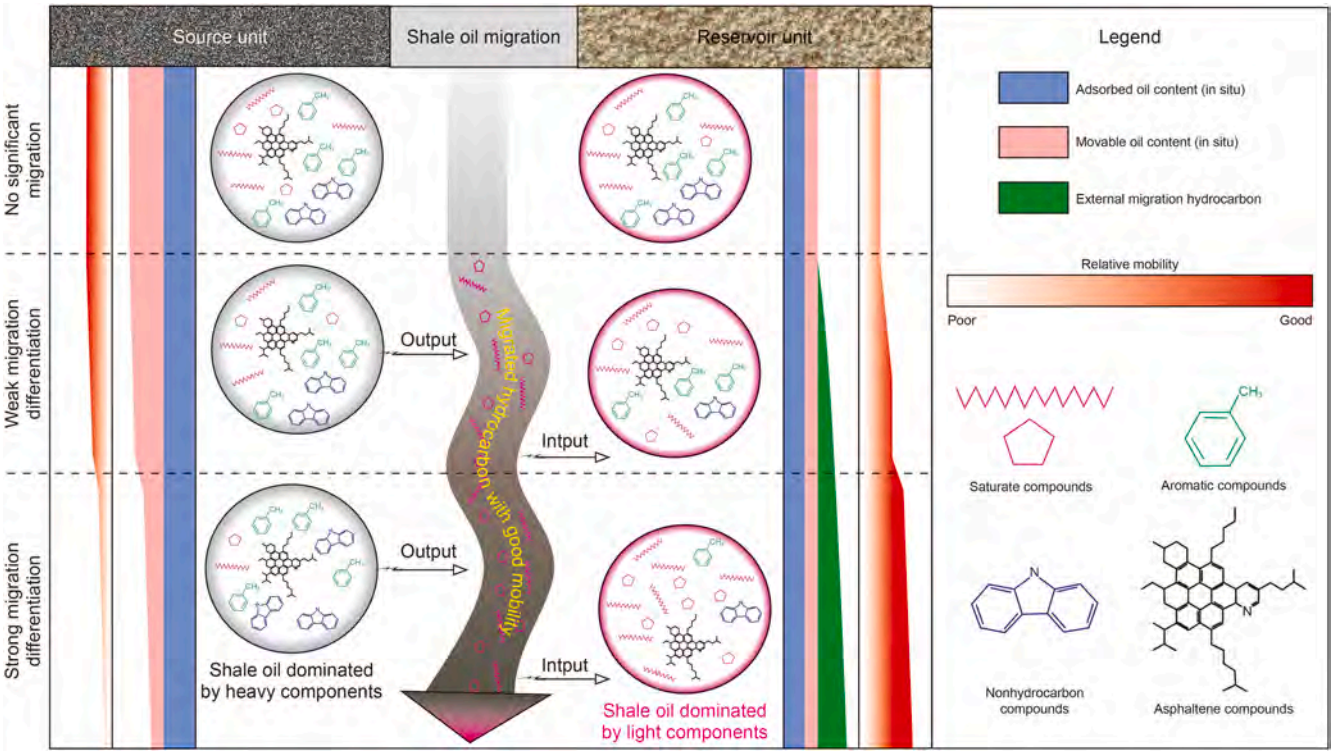

Fig. 20. Conceptual diagram showing the mobility changes of source–reservoir units under different migration intensities in shale oil systems.

components and enhanced fluidity in the FL (Fig. 11). As illustrated in Fig. 21, no significant shale oil migration across the laminae assemblage at the cm–m scale can be detected in the MS2–FLS3–MS3–FLS4 configuration; this weak migration differentiation consequently leads to highly similar shale oil mobility (reflected by OSI, movable and adsorbed oil percentages) between the source unit (i.e., MS) and reservoir unit (i.e., FLS). With respect to the FLS1–MS1–FLS2 and TLS1–FLS5–TLS2–FLS6 source–reservoir configurations, where significant shale oil migration can be detected, such strong migration differentiation ultimately contributes to a remarkable disparity in shale oil mobility between source rock units (i.e., MS and TLS) and reservoir units (i.e., FLS). Notably, reservoir units (i.e., FLS1, FLS2, FLS5, and FLS6) under conditions of strong migration differentiation generally display better mobility than those with weak or no migration differentiation, such as FLS3 and FLS4. All this evidence illustrates the controlling effect of migration differentiation strength on mobility differences between source and reservoir units in shale.

4.3. Micron- to meter-scale shale oil migration differentiation and mobility patterns

According to the μm–m-scale shale oil migration characteristics, the migration differentiation and corresponding mobility patterns in shale oil systems are established (Fig. 22). Specifically, μm–mm-scale interlaminar oil migration occurs extensively in laminated-type shale systems, which manifests as the migration of oil-generating organic-rich laminae to adjacent organic-lean laminae (e.g., FL) with favorable storage capacity. The migration differentiation and mobility changes at this scale primarily depend on the geological and geochemical disparities among the laminae. The good source–good reservoir laminated units (e.g., OL–FL) exhibit relatively strong migration differentiation and favorable mobility improvement, whereas the good source–poor reservoir laminated units (e.g., OL–TL) display weak compositional differentiation and mobility changes. Notably, this type of oil migration is not extensive in massive shales because of the absence of overlapping laminae structures. In addition, the migration distance of oil across the laminae assemblage (or lithofacies) in the shale system is greater and mainly at the cm–m scale, where the laminae assemblage (e.g., MS and TLS) with oil-generating advantages behaves as the source unit. However, the laminae assemblage (e.g., FLS) with superior storage properties is the reservoir unit. This scale migration differentiation is conducive to improving the oil mobility in reservoir units while aggravating the deterioration of oil mobility within source units, leading to a positive correlation between the migration differentiation intensity and mobility disparity of source–reservoir units. Specifically, the thick source–thick reservoir configuration results in more obvious migration differentiation and mobility improvements than the thin source–thin reservoir configuration with similar geological conditions. Compared with the shale oil that migrates at the μm–mm scale, the shale oil that migrates at the cm–m scale is lighter and has a greater degree of component differentiation and mobility variations. Overall, these organic-lean

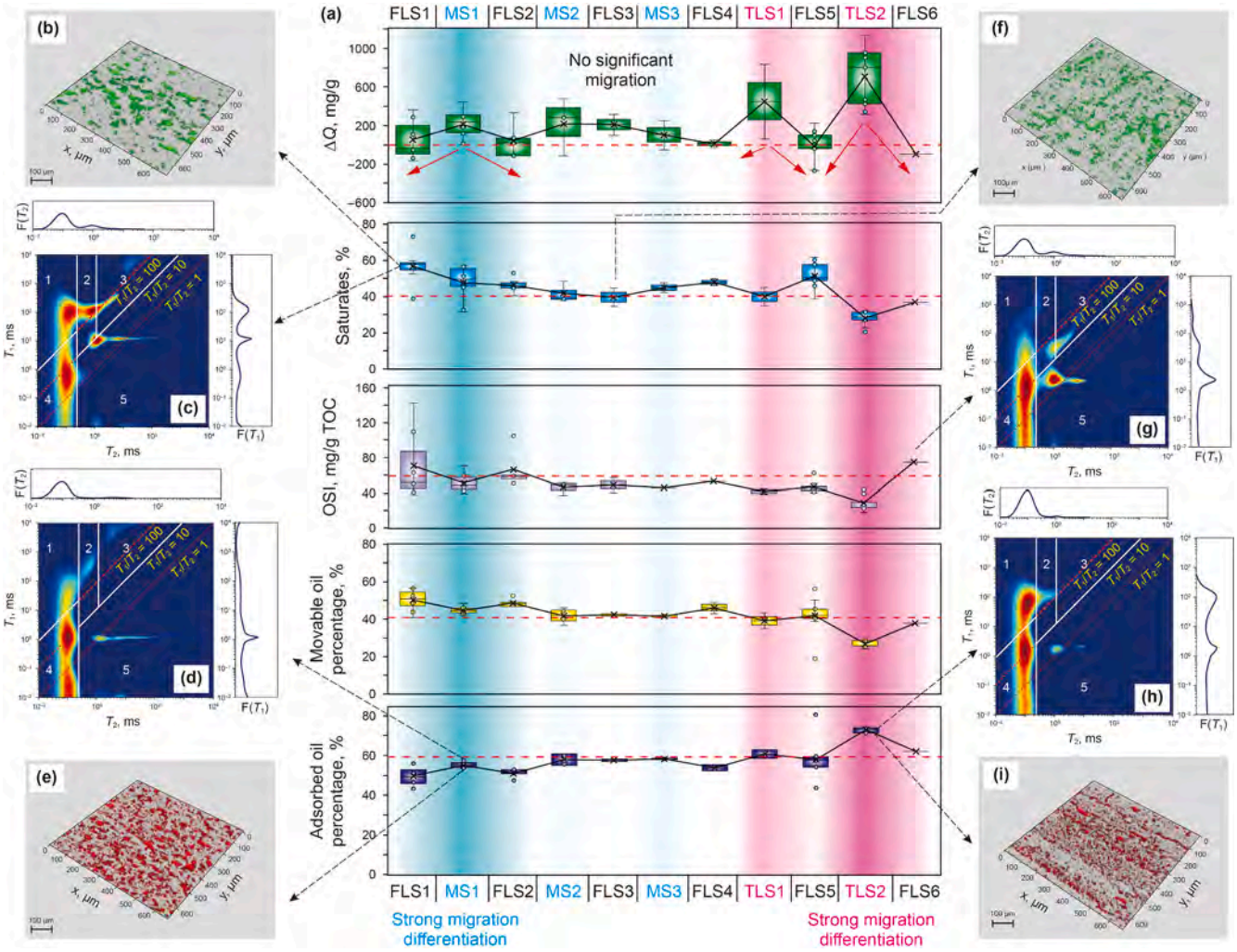

Fig. 21. **(a)** Box plot showing the Δ*Q*, saturate hydrocarbon and mobility parameters of the shale oil in the different source–reservoir units. Δ*Q* = HGPO − HGPR; HGPO = original hydrocarbon generation potential; and HGPR = true hydrocarbon generation potential. **(b)** Occurrence characteristics of the light oil component in the FLS1 unit in Well H-261 (2228.8 m). **(c)** NMR T_1–T_2 plot showing a high movable oil signal in the FLS1 unit in Well H-261 (2228.8 m). **(d)** NMR T_1–T_2 plot showing a low movable oil signal in the MS1 unit in Well H-261 (2232.0 m). **(e)** Occurrence characteristics of the heavy oil component in the MS1 unit in Well H-261 (2229.8 m). **(f)** Occurrence characteristics of the light oil component in the FLS3 unit in Well H-261 (2234.8 m). **(g)** NMR T_1–T_2 plot showing a high movable oil signal in the FLS6 unit in Well H-261 (2245.5 m). **(h)** NMR T_1–T_2 plot showing a low movable oil signal in the TLS2 unit in Well H-261 (2243.6 m). **(i)** Occurrence characteristics of the heavy oil component in the TLS2 unit in Well H-261 (2244.5 m).

shale intervals enriched with movable oil due to migration differentiation are new sweet spots that should be fully valued in future shale oil exploration projects.

4.4. Implications for high-mobility migration sweet spot evaluation

Unlike traditional *in situ* sweet spots focused on organic-rich shale formations (Glaser et al., 2013; Aldrich and Seidle, 2018), this study reveals a novel high-mobility migration sweet spot in organic-lean intervals that is more conducive to the economic recovery of shale oil. In addition to evaluating *in situ* geological and geochemical characteristics, the key to identifying migration sweet spots in shale oil systems relies on shale oil migration identification, migration differentiation intensity analysis, and favorable movable interval evaluation and prediction. In future efforts, the following procedures are recommended to scientifically evaluate migration sweet spots in shale oil systems: (1) partitioning the source–reservoir units within shale systems according to basic geological and geochemical characteristics; (2) identifying multiscale shale oil migration differentiation through multimethod combinations (e.g., LSCM, NMR, and multi-temperature pyrolysis and extraction geochemical experiments); (3) clarifying shale oil migration differentiation intensity, mobility effects, and key geological controls (e.g., source–reservoir configuration, fracture networks, and charging dynamics); and (4) evaluating and predicting migration sweet spots by combining geological–geochemical techniques, geophysical logging, and three-dimensional seismic data. These promising high-mobility migration sweet spots, combined with traditional *in situ* sweet spots, can help greatly promote the cost-effective exploration and sustainable development of shale oil resources.

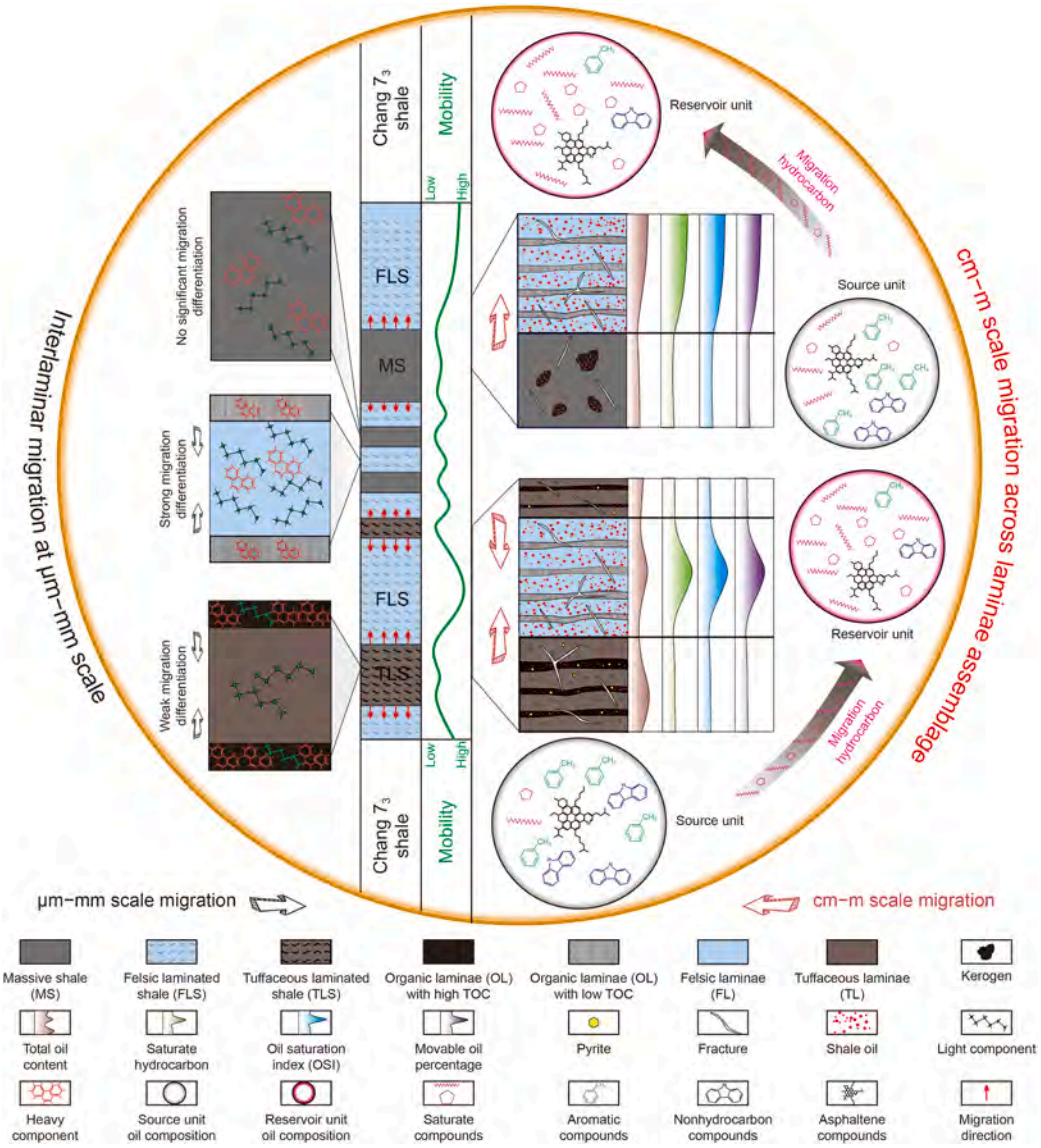

Fig. 22. Micron- to meter-scale shale oil migration differentiation and mobility patterns in the Chang 7_3 shale oil system.

5. Conclusions

In this investigation, μm–m-scale shale oil migration evidence, chemical differentiation, and corresponding mobility effects within a shale oil system were systematically evaluated by combining multiple methods and tools. This work could help clarify the intrinsic relationships among migration behavior, chemical differentiation, and mobility variations in shale oil systems, and it could be applied to evaluate high-mobility migration sweet spots that are completely different from traditional *in situ* sweet spots. The following conclusions were obtained.

(1) The μm–m-scale migration within a shale oil system essentially relies on the relative source–reservoir units with hydrocarbon generation capacity or on differences in storage capacity. The organic-rich laminae, laminae assemblages and lithofacies with poor storage capacity act primarily as source units and are dominated by the adsorption state of shale oil. Conversely, organic-lean intervals with high storage capacities behave primarily as reservoir units and present favorable oil mobility.

(2) Micrometer-scale migration in a shale oil system is manifested primarily as interlaminar migration in laminated shale, which can be identified by the detectable light/heavy component differentiation of oil via LSCM. In contrast, cm–m-scale migration is manifested mainly in the form of long distance migration across laminae assemblages or lithofacies, which can be comprehensively identified by anomalies in pyrolysis parameters (e.g., S_1/TOC, T_{max}), original–true hydrocarbon generation potential differences (i.e., $\Delta Q<0$), chemical compositions and n-alkane differentiation.

(3) The good correlation between ΔQ, compositional parameters and mobility indicators confirms that migrating hydrocarbon inputs can improve the oil composition and movable oil content, thereby affecting shale oil mobility. A saturate hydrocarbon content of 40% tends to be a critical condition where the mobility of Chang 7_3 shale oil changes significantly from a disadvantageous situation to a favorable situation. Generally, the component differentiation and mobility changes of shale oil migrating at the cm–m scale are more significant than those migrating at the μm–mm

scale because of the larger migration distance, which is more conducive to improving the fluidity of migrating hydrocarbon.

(4) The mobility disparities of different source–reservoir configuration units in a shale oil system are controlled primarily by the degree of migration differentiation. The μm–mm-scale good source–good reservoir laminated units (e.g., OL–FL) and the cm–m-scale thick source–thick reservoir configurations exhibit relatively strong migration differentiation and favorable mobility improvement. These mobility patterns associated with shale oil migration differentiation are critical for guiding future high-mobility migration sweet spot assessments and enabling cost-effective and sustainable shale oil development.

CRediT authorship contribution statement

Fu-Wei Wang: Writing – original draft, Visualization, Software, Methodology, Funding acquisition, Formal analysis, Data curation, Conceptualization. **Ru-Kai Zhu:** Supervision, Conceptualization. **Dong-Xia Chen:** Writing – review & editing, Supervision, Conceptualization. **Bin Bai:** Supervision, Conceptualization. **Chang Liu:** Visualization, Funding acquisition, Formal analysis. **Meng-Ya Jiang:** Visualization, Software. **Ren-Zeng Wanma:** Visualization, Investigation. **Qiao-Chu Wang:** Visualization, Formal analysis. **Yu-Chao Wang:** Software, Investigation. **Lan-Xi Rong:** Investigation, Formal analysis. **Yu-Qi Wang:** Software, Investigation. **Chen Liu:** Investigation. **Khawaja-Hasnain Iltaf:** Investigation. **Zhang-Xin Chen:** Supervision, Conceptualization.

Declaration of competing interest

The authors declare the following financial interests/personal relationships which may be considered as potential competing interests: On behalf of all the co-authors, we declare that they have no known competing financial interests or personal relationships that could have appeared to influence the work reported in this paper.

Acknowledgments

This work was financially supported by the National Natural Science Foundation of China (No. 42402152 and No. 42302158), the Science Foundation of China University of Petroleum (Beijing) (No. 2462023XKBH011), the CNPC Strategic Cooperation Science and Technology Special Project (No. ZLZX 2020-02-01-03), and the 2021 and 2022 AAPG Foundation Grants-in-Aid Programs. We sincerely thank PetroChina Changqing Oilfield Company for providing background geologic datasets and allowing the publication of the results. The authors would also like to thank the editor and anonymous reviewers for their valuable suggestions for improving the quality of our paper.

References

Al Duhailan, M.A., Sonnenberg, S.A., 2014. Impact of petroleum-expulsion fractures on productivity of the Bakken Shales: A geological interpretation for pressure transient behaviors. In: Unconventional Resources Technology Conference, Denver, Colorado, USA. https://doi.org/10.15530/urtec-2014-1881673.

Aldrich, J.B., Seidle, J.P., 2018. Sweet spot identification and optimization in unconventional reservoirs. Mt. Geol. 52 (3), 5–12.

Anovitz, L.M., Cole, D.R., 2015. Characterization and analysis of porosity and pore structures. Rev. Mineral. Geochem. 80 (1), 61–164. https://doi.org/10.2138/rmg.2015.80.04.

Arshadi, M., Khishvand, M., Aghaei, A., et al., 2018. Pore-scale experimental investigation of two-phase flow through fractured porous media. Water Resour. Res. 54 (5), 3602–3631. https://doi.org/10.1029/2018WR022540.

Ataman, E., Andersson, M.P., Ceccato, M., et al., 2016. Functional group adsorption on calcite: I. Oxygen containing and nonpolar organic molecules. J. Phys. Chem. C 120 (30), 16586–16596. https://doi.org/10.1021/acs.jpcc.6b01349.

Barrett, E.P., Joyner, L.G., Halenda, P.P., 1951. The determination of pore volume and area distributions in porous substances. I. Computations from nitrogen isotherms. J. Am. Chem. Soc. 73 (1), 373–380. https://doi.org/10.1021/ja01145a126.

Bennett, B., Chen, M., Brincat, D., et al., 2002. Fractionation of benzocarbazoles between source rocks and petroleums. Org. Geochem. 33 (5), 545–559. https://doi.org/10.1016/S0146-6380(02)00017-7.

Bray, E.E., Foster, W.R., 1980. A process for primary migration of petroleum. AAPG Bullet. 64 (1), 107–114. https://doi.org/10.1306/2F918937-16CE-11D7-8645000102C1865D.

Broekhoff, J.C.P., 1979. Mesopore determination from nitrogen sorption isotherms: Fundamentals, scope, limitations. In: Delmon, B., Grange, P., Jacobs, P., et al. (Eds.), Preparation of Catalysts II, Proceedings of the Second International Symposium, Studies in Surface Science and Catalysis, vol. 3. Elsevier, Amsterdam, pp. 663–684. https://doi.org/10.1016/S0167-2991(09)60243-3.

Brother, L., Engel, M.H., Krooss, B.M., 1991. The effects of fluid flow through porous media on the distribution of organic compounds in a synthetic crude oil. Org. Geochem. 17 (1), 11–24. https://doi.org/10.1016/0146-6380(91)90036-J.

Brunauer, S., Emmett, P.H., Teller, E., 1938. Adsorption of gases in multimolecular layers. J. Am. Chem. Soc. 60 (2), 309–319. https://doi.org/10.1021/ja01269a023.

Burruss, R.C., Hatch, J.R., 1989. Geochemistry of oils and hydrocarbon source rocks, Greater Anadarko Basin: Evidence for multiple sources of oils and long-distance oil migration. Anadarko Basin Symp. 90, 53–64.

Charlesworth, J.M., 1986. Interaction of clay minerals with organic nitrogen compounds released by kerogen pyrolysis. Geochem. Cosmochim. Acta 50 (7), 1431–1435. https://doi.org/10.1016/0016-7037(86)90316-9.

Clayton, J.L., Bostick, N.H., 1986. Temperature effects on kerogen and on molecular and isotopic composition of organic matter in Pierre Shale near an igneous dike. Org. Geochem. 10 (1–3), 135–143. https://doi.org/10.1016/0146-6380(86)90017-3.

Cui, J.W., Zhang, Z.Y., Liu, G.L., et al., 2022. Breakthrough pressure anisotropy and intra-source migration model of crude oil in shale. Mar. Petrol. Geol. 135, 105433. https://doi.org/10.1016/j.marpetgeo.2021.105433.

Curtis, M.E., Cardott, B.J., Sondergeld, C.H., et al., 2012. Development of organic porosity in the Woodford Shale with increasing thermal maturity. Int. J. Coal Geol. 103, 26–31. https://doi.org/10.1016/j.coal.2012.08.004.

Dai, B., Li, E.D., Wang, X.J., et al., 2021. Evaluation of shale oil migration and accumulation rules based on geochemical parameters of source rocks. Petrol. Reserv. Eval. Dev. 11 (4), 506–513. https://doi.org/10.13809/j.cnki.cn32-1825/te.2021.04.005 (in Chinese).

Dembicki Jr., H., Anderson, M.J., 1989. Secondary migration of oil: Experiments supporting efficient movement of separate, buoyant oil phase along limited conduits. AAPG Bull. 73 (8), 1018–1021. https://doi.org/10.1306/44B4A2DA-170A-11D7-8645000102C1865D.

Edman, J.D., Pitman, J.K., 2010. Geochemistry of Eagle Ford Group source rocks and oils from the first Shot field area, Texas. In: Gulf Coast Association of Geological Societies 60th Annual Convention San Antonio. Gulf Coast Association of Geological Societies, pp. 217–234.

Elsayed, M., Isah, A., Hiba, M., et al., 2022. A review on the applications of nuclear magnetic resonance (NMR) in the oil and gas industry: Laboratory and field-scale measurements. J. Pet. Explor. Prod. Technol. 12 (10), 2747–2784. https://doi.org/10.1007/s13202-022-01476-3.

Fan, Z.A., Philp, R.P., 1987. Laboratory biomarker fractionations and implications for migration studies. Org. Geochem. 11 (3), 169–175. https://doi.org/10.1016/0146-6380(87)90020-9.

Gao, Z., Bai, L., Hu, Q., et al., 2024. Shale oil migration across multiple scales: A review of characterization methods and different patterns. Earth Sci. Rev. 254, 104819. https://doi.org/10.1016/j.earscirev.2024.104819.

Gao, Z., Duan, L., Jiang, Z., et al., 2023. Using laser scanning confocal microscopy combined with saturated oil experiment to investigate the pseudo in-situ occurrence mechanism of light and heavy components of shale oil in submicron scale. J. Petrol. Sci. Eng. 220, 111234. https://doi.org/10.1016/j.petrol.2022.111234.

George, S.C., Ahmed, M., Liu, K., et al., 2004. The analysis of oil trapped during secondary migration. Org. Geochem. 35 (11–12), 1489–1511. https://doi.org/10.1016/j.orggeochem.2004.07.007.

Glaser, K.S., Miller, C.K., Johnson, G.M., et al., 2013. Seeking the sweet spot: Reservoir and completion quality in organic shales. Oilfield Rev. 25 (4), 16–29.

González-Betancourt, A.Y., González-Partida, E., Carrillo-Chávez, A., et al., 2022. Diagenetic studies of the Eagle Ford and Indidura Formations in the Sabinas Basin: Implications for source rock maturation. J. South Am. Earth Sci. 120, 104092. https://doi.org/10.1016/j.jsames.2022.104092.

Guo, Q., Yao, Y., Hou, L., et al., 2022. Oil migration, retention, and differential accumulation in "sandwiched" lacustrine shale oil systems from the Chang 7 member of the Upper Triassic Yanchang Formation, Ordos Basin, China. Int. J. Coal Geol. 261, 104077. https://doi.org/10.1016/j.coal.2022.104077.

Guo, W., Deng, S., Sun, Y., 2024. Recent advances on shale oil and gas exploration and development technologies. Adv. Geo-Energy Res. 11 (2), 81–87. https://doi.org/10.46690/ager.2024.02.01.

Guo, Z.L., Shu, C., 2013. Lattice Boltzmann Method and its Application in Engineering. Advances in Computational Fluid Dynamics, vol. 3. World Scientific. https://doi.org/10.1142/8806.
Hackley, P.C., Zhang, T., Jubb, A.M., et al., 2020. Organic petrography of Leonardian (Wolfcamp A) mudrocks and carbonates, Midland Basin, Texas: The fate of oil-prone sedimentary organic matter in the oil window. Mar. Petrol. Geol. 112, 104086. https://doi.org/10.1016/j.marpetgeo.2019.104086.
Han, Y., Horsfield, B., Mahlstedt, N., et al., 2019. Factors controlling source and reservoir characteristics in the Niobrara shale oil system, Denver Basin. AAPG Bull. 103 (9), 2045–2072. https://doi.org/10.1306/0121191619717287.
Han, Y., Mahlstedt, N., Horsfield, B., 2015. The Barnett Shale: Compositional fractionation associated with intraformational petroleum migration, retention, and expulsion. AAPG Bull. 99 (12), 2173–2202. https://doi.org/10.1306/06231514113.
Hao, F., Zou, H., Gong, Z., 2010. Preferential petroleum migration pathways and prediction of petroleum occurrence in sedimentary basins: A review. Petrol. Sci. 7 (1), 2–9. https://doi.org/10.1007/s12182-010-0001-4.
Hao, F., Zou, H., Gong, Z., et al., 2007. Petroleum migration and accumulation in the Bozhong sub-basin, Bohai Bay Basin, China: Significance of preferential petroleum migration pathways (PPMP) for the formation of large oilfields in lacustrine fault basins. Mar. Petrol. Geol. 24 (1), 1–13. https://doi.org/10.1016/j.marpetgeo.2006.10.007.
Hawthorne, S.B., Miller, D.J., Kukowski, K., et al., 2021. Turtles and snakes: Evidence for molecular shape-selective migration of crude oil hydrocarbons in the Bakken Petroleum System. Energy Fuel. 35 (13), 10584–10596. https://doi.org/10.1021/acs.energyfuels.1c01324.
He, W.Y., Meng, Q., Feng, Z.H., et al., 2022. In-situ accumulation theory and exploration & development practice of Gulong shale oil in Songliao Basin. Acta Pet. Sin. 43 (1), 1–14. https://doi.org/10.7623/syxb202201001 (in Chinese).
Hong, X., Yu, H., Xu, H., et al., 2022. Competitive adsorption of asphaltene and n-heptane on quartz surfaces and its effect on crude oil transport through nanopores. J. Mol. Liq. 359, 119312. https://doi.org/10.1016/j.molliq.2022.119312.
Hosseini, M., Arif, M., Keshavarz, A., et al., 2021. Neutron scattering: A subsurface application review. Earth Sci. Rev. 221, 103755. https://doi.org/10.1016/j.earscirev.2021.103755.
Hu, S.Z., Li, S.F., Xia, L.W., et al., 2020. On the internal oil migration in shale systems and implications for shale oil accumulation: A combined petrological and geochemical investigation in the Eocene Nanxiang Basin, China. J. Petrol. Sci. Eng. 184, 106493. https://doi.org/10.1016/j.petrol.2019.106493.
Hu, T., Jiang, F., Pang, X., et al., 2024a. Identification and evaluation of shale oil micro-migration and its petroleum geological significance. Petrol. Explor. Dev. 51 (1), 127–140. https://doi.org/10.1016/S1876-3804(24)60010-8.
Hu, T., Jing, Z., Zhang, Q., et al., 2025. Shale oil micro-migration characterization: Key methods and outlook. Adv. Geo-Energy Res. 15 (1), 5–12. https://doi.org/10.46690/ager.2025.01.02.
Hu, T., Liu, Y., Jiang, F., et al., 2024b. A novel method for quantifying hydrocarbon micromigration in heterogeneous shale and the controlling mechanism. Energy 288, 129712. https://doi.org/10.1016/j.energy.2023.129712.
Hu, W.X., Kang, X., Cao, J., et al., 2018. Thermochemical oxidation of methane induced by high-valence metal oxides in a sedimentary basin. Nat. Commun. 9, 5131. https://doi.org/10.1038/s41467-018-07267-x.
Hwang, R.J., Heidrick, T., Mertani, B., et al., 2002. Correlation and migration studies of North Central Sumatra oils. Org. Geochem. 33 (12), 1361–1379. https://doi.org/10.1016/S0146-6380(02)00104-3.
Jarvie, D.M., 2012. Shale resource systems for oil and gas: Part 2 shale-oil resource systems. In: Breyet, J. (Ed.), Shale Reservoirs—Giant Resources for the 21st Century, vol. 97. AAPG Memoir, pp. 89–119. https://doi.org/10.1306/13321447M973489.
Jarvie, D.M., 2014. Components and processes affecting producibility and commerciality of shale resource systems. Geol. Acta 12 (4), 307–325. https://doi.org/10.1344/GeologicaActa2014.12.4.3.
Jarvie, D.M., Coskey, R.J., Johnson, M.S., et al., 2011. The geology and geochemistry of the Parshall area, Mountrail County, North Dakota. In: Robinson, J.W., LeFever, J.A., Gaswirth, S.B. (Eds.), The Bakken-three Forks Petroleum System in the Williston Basin. Rocky Mountain Association of Geologists, Denver, Colorado, pp. 229–268.
Jiang, Q.G., Li, M.W., Qian, M.H., et al., 2016. Quantitative characterization of shale oil in different occurrence states and its application. Petrol. Geol. Exp. 38 (6), 842–849. https://doi.org/10.11781/sysydz201606842 (in Chinese).
Ko, L.T., Loucks, R.G., Ruppel, S.C., et al., 2017. Origin and characterization of Eagle Ford pore networks in the South Texas Upper Cretaceous shelf. AAPG Bull. 101 (3), 387–418. https://doi.org/10.1306/08051616035.
Krooss, B.M., Brothers, L., Engel, M.H., 1991. Geochromatography in petroleum migration: A review. Geol. Soc. Spec. Publ. 59 (1), 149–163. https://doi.org/10.1144/GSL.SP.1991.059.01.11.
Lafargue, W., Espitalie, J., Broks, T.M., et al., 1994. Experimental simulation of primary migration. Org. Geochem. 22 (3–5), 575–586. https://doi.org/10.1016/0146-6380(94)90126-0.
Larter, S.R., Bowler, B.F.J., Li, M., et al., 1996. Molecular indicators of secondary oil migration distances. Nature 383 (6601), 593–597. https://doi.org/10.1038/383593a0.
Leythaeuser, D., Schaefer, R.G., Cornford, C.T., et al., 1979. Generation and migration of light hydrocarbons (C_2–C_7) in sedimentary basins. Org. Geochem. 1 (4), 191–204. https://doi.org/10.1016/0146-6380(79)90022-6.
Leythaeuser, D., Schaefer, R.G., Yukler, A., 1982. Role of diffusion in primary migration of hydrocarbons. AAPG Bull. 66 (4), 408–429. https://doi.org/10.1306/03B59B2A-16D1-11D7-8645000102C1865D.
Li, J., 2020. Study on Occurrence Mechanism and Mobility of Shale Oil: A Case Study of Shahejie Formation in Jiyang Depression. Ph. D. thesis. Qingdao: China University of Petroleum (East China) (in Chinese).
Li, J., Jiang, C., Wang, M., et al., 2020. Adsorbed and free hydrocarbons in unconventional shale reservoir: A new insight from NMR T_1–T_2 maps. Mar. Petrol. Geol. 116, 104311. https://doi.org/10.1016/j.marpetgeo.2020.104311.
Li, M., Chen, Z., Cao, T., et al., 2018. Expelled oils and their impacts on Rock-Eval data interpretation, Eocene Qianjiang Formation in Jianghan Basin, China. Int. J. Coal Geol. 191, 37–48. https://doi.org/10.1016/j.coal.2018.03.001.
Li, Z., Zou, Y.R., Xu, X.Y., et al., 2016. Adsorption of mudstone source rock for shale oil—Experiments, model and a case study. Org. Geochem. 92, 55–62. https://doi.org/10.1016/j.orggeochem.2015.12.009.
Liang, C., Wu, J., Cao, Y.C., et al., 2022. Storage space development and hydrocarbon occurrence model controlled by lithofacies in the Eocene Jiyang Subbasin, East China: Significance for shale oil reservoir formation. J. Petrol. Sci. Eng. 215, 110631. https://doi.org/10.1016/j.petrol.2022.110631.
Liu, B., Bai, L.H., Chi, Y.A., et al., 2019. Geochemical characterization and quantitative evaluation of shale oil reservoir by two-dimensional nuclear magnetic resonance and quantitative grain fluorescence on extract: A case study from the Qingshankou Formation in Southern Songliao Basin, Northeast China. Mar. Petrol. Geol. 109, 561–573. https://doi.org/10.1016/j.marpetgeo.2019.06.046.
Liu, Z., Liu, D., Cai, Y., et al., 2020. Application of nuclear magnetic resonance (NMR) in coalbed methane and shale reservoirs: A review. Int. J. Coal Geol. 218, 103261. https://doi.org/10.1016/j.coal.2019.103261.
Lowell, S., Shields, J.E., Thomas, M.A., et al., 2004. Characterization of Porous Solids and Powders: Surface Area, Pore Size and Density. Particle Technology Series vol. 16. Springer Science & Business Media. https://doi.org/10.1007/978-1-4020-2303-3.
Ma, X., Li, M., Pang, X., et al., 2019. Paradox in bulk and molecular geochemical data and implications for hydrocarbon migration in the inter-salt lacustrine shale oil reservoir, Qianjiang Formation, Jianghan Basin, central China. Int. J. Coal Geol. 209, 72–88. https://doi.org/10.1016/j.coal.2019.05.005.
Mastalerz, M., Drobniak, A., Hower, J.C., 2021. Controls on reservoir properties in organic-matter-rich shales: Insights from MICP analysis. J. Petrol. Sci. Eng. 196, 107775. https://doi.org/10.1016/j.petrol.2020.107775.
McAuliffe, C.D., 1979. Oil and gas migration: Chemical and physical constraints. AAPG Bull. 63 (5), 761–781. https://doi.org/10.1306/2F9182CF-16CE-11D7-8645000102C1865D.
Milliken, K.L., Rudnicki, M., Awwiller, D.N., et al., 2013. Organic matter-hosted pore system, Marcellus Formation (Devonian), Pennsylvania. AAPG Bull. 97 (2), 177–200. https://doi.org/10.1306/07231212048.
National Energy Administration, 2016. SY/T5119–2016: Ananlysis Mothed for Family Composition of Rock Extracts and Crude Oil.
National Standards Complication Group of People's Republic of China, 2012. GB/T 18602–2012: Rock Pyrolysis Analysis, National Standard Method. China Standard Press, Beijing.
Poetz, S., Kuske, S., Song, Y., et al., 2020. Using polar nitrogen-, sulphur-and oxygen-compound compositions from ultra-high resolution mass spectrometry for petroleum fluid assessment in the Eagle Ford Formation, Texas. Geol. Soc. Spec. Publ. 484, 71–96. https://doi.org/10.1144/SP484-2018-175.
Schowalter, T.T., 1979. Mechanics of secondary hydrocarbon migration and entrapment. AAPG Bull. 63 (5), 723–760. https://doi.org/10.1306/2F9182CA-16CE-11D7-8645000102C1865D.
Simonet, B.R.T., Brenner, S., Peters, K.E., et al., 1981. Thermal alteration of Cretaceous black shale by diabase intrusions in the Eastern Atlantic: II. Effects on bitumen and kerogen. Geochem. Cosmochim. Acta 45 (9), 1581–1602. https://doi.org/10.1016/0016-7037(81)90287-8.
Sing, K.S.W., 1985. Reporting physisorption data for gas/solid systems with special reference to the determination of surface area and porosity (recommendations 1984). Pure Appl. Chem. 57 (4), 603–619. https://doi.org/10.1351/pac198557040603.
Sivan, P., Datta, G.C., Singh, R.R., 2008. Aromatic biomarkers as indicators of source, depositional environment, maturity and secondary migration in the oils of Cambay Basin, India. Org. Geochem. 39 (11), 1620–1630. https://doi.org/10.1016/j.orggeochem.2008.06.009.
Stainforth, J.G., Reinders, J.E.A., 1990. Primary migration of hydrocarbons by diffusion through organic matter networks, and its effect on oil and gas generation. Org. Geochem. 16 (1–3), 61–74. https://doi.org/10.1016/0146-6380(90)90026-V.
Sun, M., Fu, J., Wang, Q., et al., 2024. Pore network characterization and fluid occurrence of shale reservoirs: State-of-the-art and future perspectives. Adv. Geo-Energy Res. 12 (3), 161–167. https://doi.org/10.46690/ager.2024.06.01.
Sun, M., Zhao, J., Pan, Z., et al., 2020. Pore characterization of shales: A review of small angle scattering technique. J. Nat. Gas Sci. Eng. 78, 103294. https://doi.org/10.1016/j.jngse.2020.103294.
Tao, S.Z., Hu, S.Y., Wang, J., et al., 2023. Forming conditions, enrichment regularities and resource potentials of continental tight oil in China. Acta Pet. Sin. 44 (8), 1222–1239. https://doi.org/10.7623/syxb202308003 (in Chinese).
Thommes, M., Kaneko, K., Neimark, A.V., et al., 2015. Physisorption of gases, with special reference to the evaluation of surface area and pore size distribution

(IUPAC Technical Report). Pure Appl. Chem. 87 (9–10), 1051–1069. https://doi.org/10.1515/pac-2014-1117.
Vanini, G., Barra, T.A., Souza, L.M., et al., 2020. Characterization of nonvolatile polar compounds from Brazilian oils by electrospray ionization with FT-ICR MS and Orbitrap-MS. Fuel 282, 118790. https://doi.org/10.1016/j.fuel.2020.118790.
Wang, F., Chen, D., Yao, D., et al., 2022b. Disparities in tight sandstone reservoirs in different source-reservoir assemblages and their effect on tight oil accumulation: Triassic Chang 7 member in the Qingcheng area, Ordos Basin. J. Petrol. Sci. Eng. 217, 110914. https://doi.org/10.1016/j.petrol.2022.110914.
Wang, F.W., Chen, D.X., Jiang, M.Y., et al., 2025. Multi-scale migration mechanism, accumulation effect and enrichment mode of tight oil reservoir in the Member 7 of Yanchang Formation in Jiyuan area, Ordos Basin. Acta Pet. Sin. 46 (6), 1126–1143. https://doi.org/10.7623/syxb202506007 (in Chinese).
Wang, F.W., Chen, D.X., Xie, G.J., et al., 2022a. Differential enrichment mechanism of tight sandstone oil under the control of the source-reservoir structures of Member 7 of Yanchang Formation in Qingcheng area, Ordos Basin. Acta Pet. Sin. 43 (7), 941–956. https://doi.org/10.7623/syxb202207005 (in Chinese).
Wang, M., Ma, R., Li, J.B., et al., 2019. Occurrence mechanism of lacustrine shale oil in the Paleogene Shahejie Formation of Jiyang Depression, Bohai Bay Basin, China. Petrol. Explor. Dev. 46 (4), 833–846. https://doi.org/10.1016/S1876-3804(19)60242-9.
Wang, Y., Cao, J., Tao, K., et al., 2020. Reevaluating the source and accumulation of tight oil in the Middle Permian Lucaogou Formation of the Junggar Basin. China. Mar. Petrol. Geol. 117, 104384. https://doi.org/10.1016/j.marpetgeo.2020.104384.
Wang, Y., Cheng, H., 2023. Advances in microscopic pore structure characterization of fine-grained mudrocks. Energy Fuel. 37 (3), 1495–1510. https://doi.org/10.1021/acs.energyfuels.2c03144.
Xiong, Q.R., Baychev, T.G., Jivkov, A.P., 2016. Review of pore network modelling of porous media: Experimental characterisations, network constructions and applications to reactive transport. J. Contam. Hydrol. 192, 101–117. https://doi.org/10.1016/j.jconhyd.2016.07.002.
Yuan, M., Pan, S.Q., Jing, Z.H., et al., 2023. Geochemical distortion on shale oil maturity caused by oil migration: Insights from the non-hydrocarbons revealed by FT-ICR MS. Int. J. Coal Geol. 266, 104142. https://doi.org/10.1016/j.coal.2022.104142.
Zhang, J.Y., Zhu, R.K., Wu, S.T., et al., 2023. Microscopic oil occurrence in high-maturity lacustrine shales: Qingshankou Formation, Gulong Sag, Songliao Basin. Petrol. Sci. 20, 2726–2746. https://doi.org/10.1016/j.petsci.2023.08.026.
Zhang, L., Li, M., Wang, Y., et al., 2013. A novel molecular index for secondary oil migration distance. Sci. Rep. 3, 2487. https://doi.org/10.1038/srep02487.
Zhang, T.W., Wang, X.Z., Zhang, J.F., et al., 2017. Geochemical evidence for oil and gas expulsion in Triassic lacustrine organic-rich mudstone, Ordos Basin, China. Interpretation 5 (2), SF41–SF61. https://doi.org/10.1190/INT-2016-0104.1.
Zhang, Y., Chang, J., Jiang, Z., et al., 2024. Visualization of dynamic micro-migration of shale oil and investigation of shale oil movability by NMRI combined oil charging/water flooding experiments: A novel approach. Mar. Petrol. Geol. 165, 106907. https://doi.org/10.1016/j.marpetgeo.2024.106907.
Zhang, Y.N., Fang, T.M., Li, R.C., et al., 2020. Molecular insight into the oil charging mechanism in tight reservoirs. Chem. Eng. Sci. 211, 115297. https://doi.org/10.1016/j.ces.2019.115297.
Zhao, J.L., Qin, F.F., Derome, D., et al., 2020a. Simulation of quasi-static drainage displacement in porous media on pore-scale: coupling lattice Boltzmann method and pore network model. J. Hydrol. 588, 125080. https://doi.org/10.1016/j.jhydrol.2020.125080.
Zhao, X., Sun, M., Ukaomah, C.F., et al., 2023. Pore connectivity and microfracture characteristics of Longmaxi shale in the Fuling gas field: Insights from mercury intrusion capillary pressure analysis. Gas Sci. Eng. 119, 205134. https://doi.org/10.1016/j.jgsce.2023.205134.
Zhao, Y.L., Lu, G., Zhang, L.H., et al., 2020b. Physical simulation of waterflooding development in large-scale fractured-vuggy reservoir considering filling characteristics. J. Petrol. Sci. Eng. 191, 107328. https://doi.org/10.1016/j.petrol.2020.107328.
Zheng, M., Li, J.Z., Wu, X.Z., et al., 2016. Physical modeling of oil charging in tight reservoirs: A case study of Permian Lucaogou Formation in Jimsar Sag, Junggar Basin, NW China. Petrol. Explor. Dev. 43 (2), 241–250. https://doi.org/10.1016/S1876-3804(16)30027-1.
Zhu, C., Gang, W., Zhao, X., et al., 2020. The preferential pathways of oil migration in the Qi-Nan slope belt of Bohai Bay Basin, China: Insights from integrated analyses using geochemical and morphology tools. J. Petrol. Sci. Eng. 193, 107451. https://doi.org/10.1016/j.petrol.2020.107451.
Zou, C., Pan, S., Horsfield, B., et al., 2019. Oil retention and intrasource migration in the organic-rich lacustrine Chang 7 shale of the Upper Triassic Yanchang Formation, Ordos Basin, central China. AAPG Bull. 103 (11), 2627–2663. https://doi.org/10.1306/01301917052.